Article

Neuron

Bayesian Computation through Cortical Latent Dynamics

Graphical Abstract

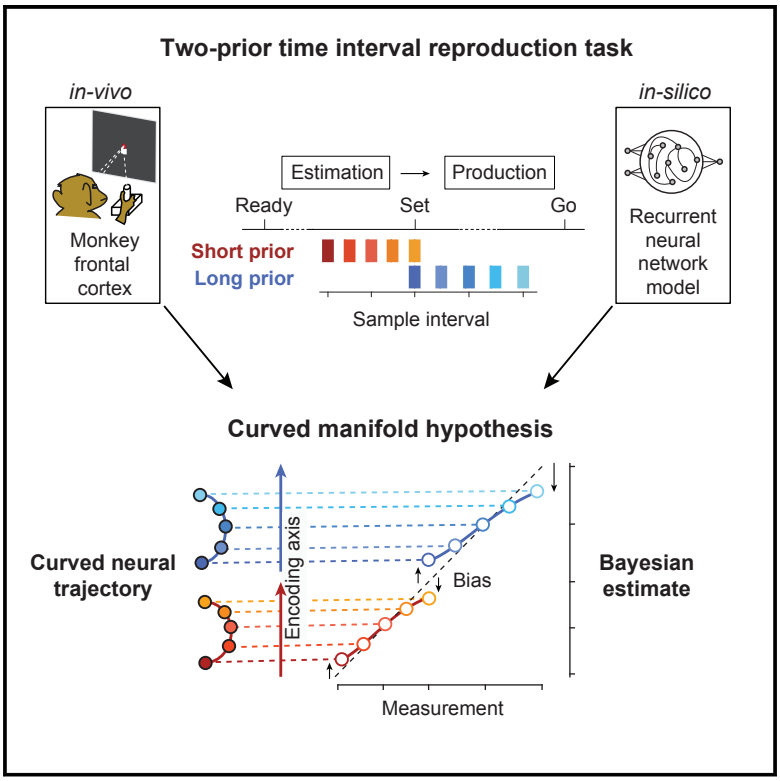

Highlights

- Monkeys estimate time by integrating sensory evidence with prior beliefs
- Prior beliefs warp neural representations in the frontal cortex
- Warped representations provide an optimal substrate for integrating beliefs
- Recurrent neural network models validate the warping effect of prior beliefs

Authors

Hansem Sohn, Devika Narain, Nicolas Meirhaeghe, Mehrdad Jazayeri

Correspondence

mjaz@mit.edu

In Brief

Sohn et al. found that prior beliefs warp neural representations in the frontal cortex. This warping provides a substrate for the optimal integration of prior beliefs with sensory evidence during sensorimotor behavior.

Sohn et al., 2019, Neuron *103*, 934–947
September 4, 2019
https://doi.org/10.1016/j.neuron.2019.06.012

CellPress

CellPress

Neuron
Article

Bayesian Computation through Cortical Latent Dynamics

Hansem Sohn,[1,4] Devika Narain,[1,3,4] Nicolas Meirhaeghe,[2,4] and Mehrdad Jazayeri[1,5,*]
[1]Department of Brain and Cognitive Sciences, McGovern Institute for Brain Research, Massachusetts Institute of Technology, Cambridge, MA 02139, USA
[2]Harvard-MIT Division of Health Sciences and Technology, Cambridge, MA 02139, USA
[3]Erasmus Medical Center, Rotterdam 3015CN, the Netherlands
[4]These authors contributed equally
[5]Lead Contact
*Correspondence: mjaz@mit.edu
https://doi.org/10.1016/j.neuron.2019.06.012

SUMMARY

Statistical regularities in the environment create prior beliefs that we rely on to optimize our behavior when sensory information is uncertain. Bayesian theory formalizes how prior beliefs can be leveraged and has had a major impact on models of perception, sensorimotor function, and cognition. However, it is not known how recurrent interactions among neurons mediate Bayesian integration. By using a time-interval reproduction task in monkeys, we found that prior statistics warp neural representations in the frontal cortex, allowing the mapping of sensory inputs to motor outputs to incorporate prior statistics in accordance with Bayesian inference. Analysis of recurrent neural network models performing the task revealed that this warping was enabled by a low-dimensional curved manifold and allowed us to further probe the potential causal underpinnings of this computational strategy. These results uncover a simple and general principle whereby prior beliefs exert their influence on behavior by sculpting cortical latent dynamics.

INTRODUCTION

Past experiences impress upon neural circuits information about statistical regularities in the environment, which help us in types of behavior, from reaching for one's back pocket to making inferences about others' mental states. There is, however, a fundamental gap in our understanding of how behavior exploits statistical regularities in relation to how the nervous system represents past experiences. The effect of statistical regularities on behavior is often described in terms of Bayesian theory, which offers a principled framework for understanding the combined effect of prior beliefs and sensory evidence in perception (Knill and Richards, 1996), cognition (Griffiths et al., 2008), and sensorimotor function (Körding and Wolpert, 2004). On the other hand, the effects of experience on neural activity have been described in terms of cellular mechanisms that govern the response properties of neurons. For example, natural statistics are thought to shape response properties of early sensory neurons through adjustments of synaptic connections (Girshick et al., 2011; Simoncelli and Olshausen 2001; Berkes et al., 2011; Fiser et al., 2010). Single-unit responses in many brain areas are thought to encode recent sensory events (Akrami et al., 2018), motor responses (Darlington et al., 2018; Gold et al., 2008; Janssen and Shadlen, 2005), reward expectations (Platt and Glimcher, 1999; Seo et al., 2014; Sugrue et al., 2004), and temporal contingencies (Narain et al., 2018). However, an understanding of how experience-dependent neural representations enable Bayesian computations is lacking.

Recent studies have focused on an analysis of the structure of *in vivo* cortical activity in trained animals and *in silico* activity in trained recurrent neural networks (RNNs) to gain a deeper understanding of how neural populations perform computations (Churchland et al., 2012; Chaisangmongkon et al., 2017; Mante et al., 2013; Remington et al., 2018a; Wang et al., 2018; Yang et al., 2019). Following this emerging multidisciplinary approach, we analyzed the structure of neural activity in the frontal cortex of monkeys and *in silico* activity in RNNs in a Bayesian timing task. Results provided evidence that prior statistics establish curved manifolds of neural activity that warp the underlying representations of time and cause biases in behavioral responses in accordance with Bayes-optimal integration.

RESULTS

Task and Behavior

Two rhesus macaques performed a time-interval reproduction task, which we refer to as the Ready-Set-Go (RSG) task (Figure 1A). The task consists of an estimation epoch followed by a production epoch. In the estimation epoch, animals had to estimate a sample interval, t_s, demarcated by two visual flashes (Ready followed by Set). In the production epoch, animals had to produce a matching interval by either initiating a saccade or by moving the joystick to the left or right (Go), depending on the location of a peripheral target. Monkeys received a reward if the produced interval, t_p, between Set and Go was sufficiently close to t_s (Figure 1B).

We manipulated the animals' prior expectations by sampling t_s from one of two uniform prior distributions, a "Short" prior

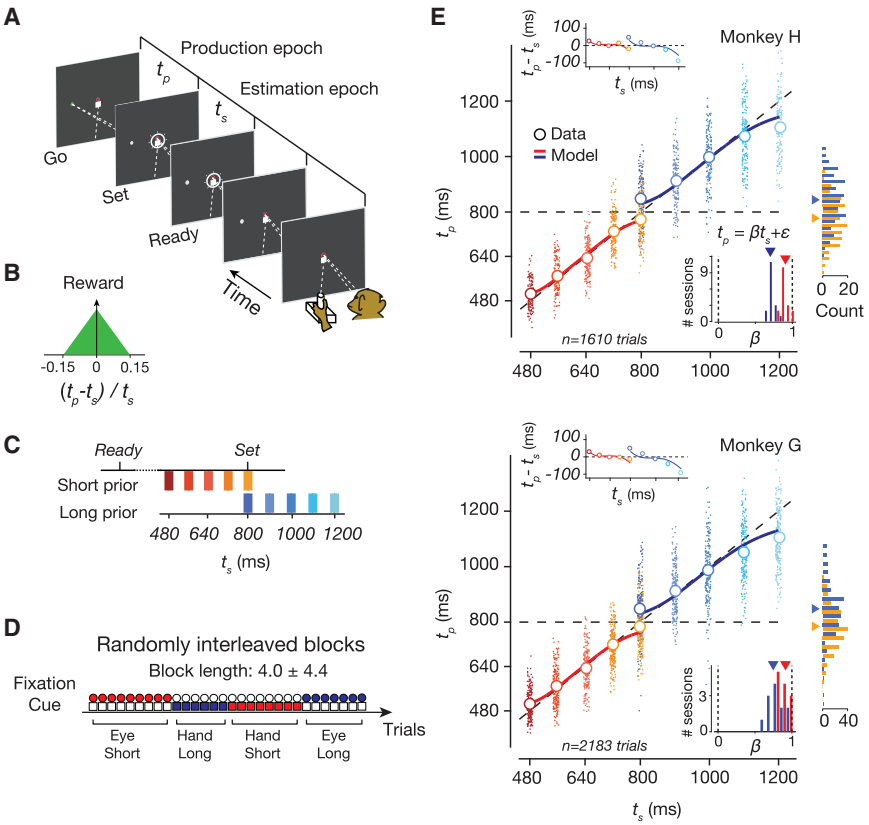

Figure 1. Task and Behavior

(A) Schematic of a single trial of the Ready-Set-Go task. The animal has to estimate a sample interval, t_s, between Ready and Set (estimation epoch), and produce a matching interval, t_p, after Set with a delayed response (Go) via a saccade or a movement of the joystick (production epoch).

(B) Reward as a function of relative error $(t_p - t_s) / t_s$.

(C) Short and Long prior distributions of t_s.

(D) Eight randomly interleaved trial types (see STAR Methods): 2 prior conditions (Short and Long) × 2 effectors (Eye and Hand) × 2 target directions (Left and Right). Mean and SD of block length is shown.

(E) Behavior. Top: a representative session for monkey H showing t_p pooled across effectors and target directions (small dots, individual trials; large open circles, average t_p per t_s; solid lines, Bayesian model; diagonal, unity line). The horizontal location of dots was jittered to facilitate visualization. Right: histograms of t_p for the overlapping t_s (horizontal dashed line) for the two prior conditions (orange, Short; blue, Long; triangles, averages). Top-left inset: average error (i.e., bias) for each t_s (circles, data; solid lines, Bayesian model). Bottom-right inset: histogram of regression slopes relating t_p to t_s across sessions (red, Short; blue, Long; triangles, averages). Bottom: the same as top for monkey G.

ranging between 480 and 800 ms, and a "Long" prior ranging between 800 and 1,200 ms (Figure 1C). The task enabled us to also manipulate sensory uncertainty since measurements of time intervals become more variable for longer intervals, a property known as "scalar variability" (Malapani and Fairhurst, 2002). Since the two prior distributions overlapped at t_s = 800 ms, the task further offered the opportunity to characterize how neural representations are independently modulated by prior beliefs. The prior condition and the desired effector were switched across short blocks of trials (block length: 4.0 ± 4.4 trials; uniform hazard) and the trial type was explicitly cued throughout each trial (Figure 1D). The rationale for including two response modalities and two directions of response was to ensure that the neural correlates of Bayesian integration identified would generalize across multiple experimental conditions.

To verify that animals learned to perform the task, we used a regression analysis to assess the dependence of t_p on t_s. The regression slopes were positive, indicating that animals were able to estimate t_s and were less than unity, indicating that responses were biased toward the mean of the prior (Figures 1E and S1; Table S1). The effect of the prior was most conspicuous at the overlapping t_s for which biases were in opposite directions for the two prior conditions (rank-sum test, $p < 10^{-43}$ in animal H, $p < 10^{-75}$ in G; Figure 1E; Table S2). This effect was present immediately after block transitions (Figure S2), indicating that animals rapidly switched between priors. These results indicate that animals learned the task contingencies and relied on their prior expectation of t_s.

Next, we used a Bayesian observer model to analyze the behavior (Figure 2A). Assuming that measurement noise scales with the interval (Malapani and Fairhurst, 2002) and that the observer relies on the experimentally imposed uniform prior, the behavior of the model is captured by a sigmoidal function that maps noisy measurements, t_m, to optimal estimates, t_e (Jazayeri and Shadlen, 2010). This model makes three predictions. First, it predicts the tradeoff between response bias and variance. Accordingly, fits of the model to behavior captured the bias and variance (Figures 2C and 2D) for both animals and across all experimental conditions (Figure S1; Table S3). Second, the model predicts larger biases for intervals near the two ends of the distribution (Figure 2E). Consistent with this prediction, t_p increments at the extrema of the prior were smaller than increments near the mean (signed-rank test, $p < 10^{-11}$ in animal H, $p < 10^{-12}$ in G; Figure 2F; see Figure S1 for another test of sigmoidal behavior). Third, due to scalar variability, biases for the Long prior should be larger than the Short prior condition (Figure 2G), which we confirmed empirically (Figure 2H; Table S1). Together, these results provide strong evidence that animals used a Bayesian strategy to perform the RSG task.

Single-Neuron Response Profiles

We recorded neural activity in the dorsomedial frontal cortex (DMFC) including the supplementary eye field (SEF), the dorsal region of the supplementary motor area (SMA), and pre-SMA. Our choice of recording areas was motivated by previous work showing a central role for DMFC in motor timing, movement

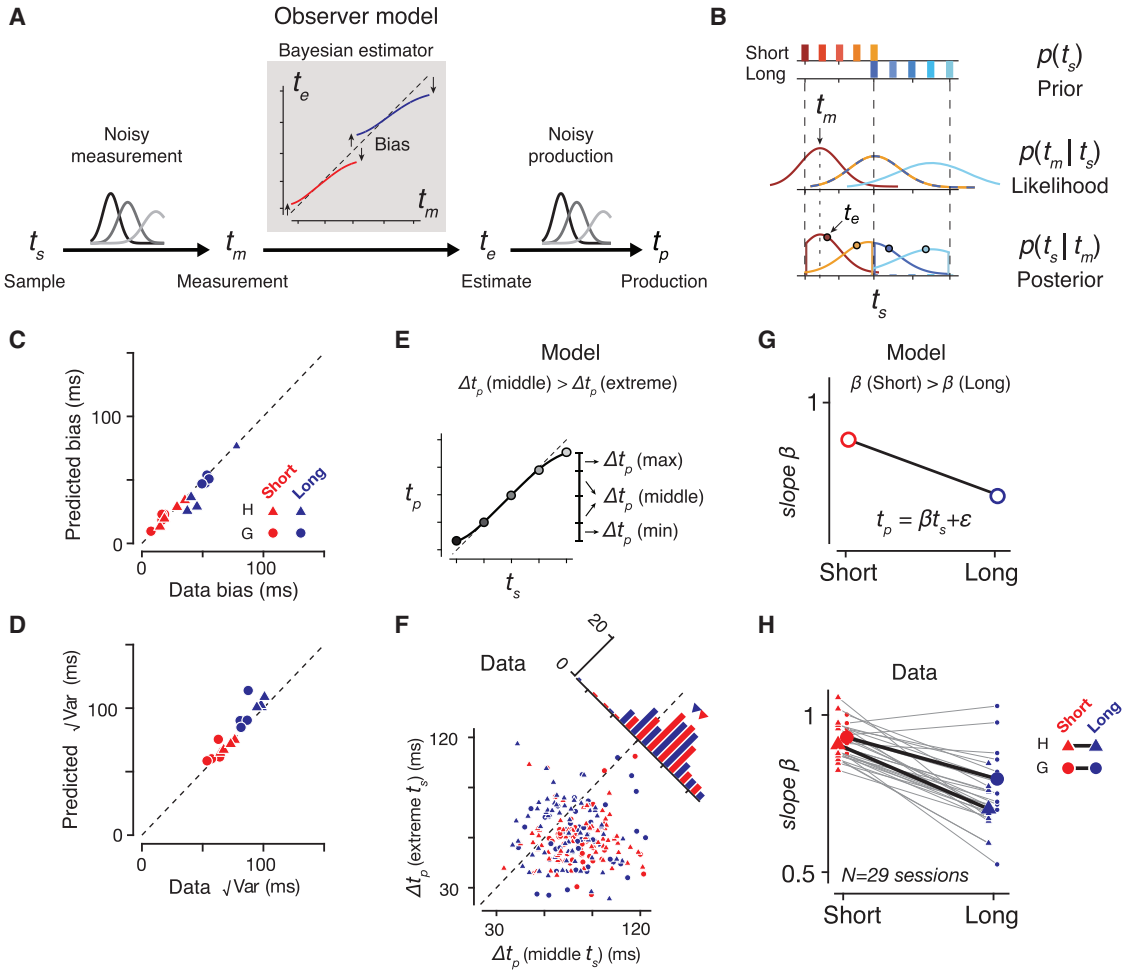

Figure 2. Bayesian Model and Behavior

(A) Bayesian observer model. The measurement (t_m) is the sample interval (t_s) plus white noise with SD proportional to t_s. The Bayesian estimator is a sigmoidal function that maps t_m to an optimal estimate (t_e) (red, Short; blue, Long). t_e is biased toward the mean of the prior (arrows). The production interval (t_p) is t_e plus scalar noise during production epoch.

(B) The prior (top), the likelihood function (middle), the resulting posterior (bottom), and the posterior mean (circles) that represent the estimate.

(C) Comparison of t_p bias relative to t_s between model and behavior across animals and conditions.

(D) Same as (C) for variability. Individual trials were pooled across sessions for each condition to compute the variance.

(E) The sigmoidal Bayesian estimator predicts that the average t_p difference across neighboring t_s (Δt_p) should be larger around the mean of the prior distribution (Δt_p(middle)), compared to its extrema, Δt_p (extreme) (average of Δt_p(max) and Δt_p(min)).

(F) Δt_p (extreme) as a function Δt_p (middle) for each session and condition (prior, response modality, direction) pooled across the two monkeys. Each data point represents a session (red, Short; blue, Long). Top-right: histogram of the difference between Δt_p(middle) and Δt_p(extreme). The difference was similar between Short and Long (red and blue triangles) as predicted by the model. Triangles shows averages across datasets. See also Figure S1.

(G) Model prediction for bias for the two prior conditions.

(H) Slopes of regression lines relating t_p to t_s for individual sessions (small markers connected by gray lines) and the corresponding averages (big markers connected by a black line). Triangles represent monkey H, and circles, monkey G.

planning, and learning in humans (Coull et al., 2004; Cui et al., 2009; Halsband et al., 1993), monkeys (Chen and Wise, 1996; Histed and Miller, 2006; Lara et al., 2018; Lu et al., 2002; Merchant et al., 2013; Mita et al., 2009; Ohmae et al., 2008; Schall et al., 2002), and rodents (Emmons et al., 2017; Kim et al., 2013; Matell et al., 2003; Murakami et al., 2014).

During the estimation epoch, many neurons had heterogeneous response profiles that were modulated by elapsed time in a prior-dependent fashion (Figure 3A). Consequently, responses at the time of Set varied with both the prior and t_s (Figure 3B). The presentation of Set triggered a transient modulation of firing rates (Figure 3Bi-iii,v). Following this transient, neurons exhibited a range of monotonic (e.g., ramping) or non-monotonic response profiles that were often organized according to t_s irrespective of the prior condition (Figure 3Bi-iii,vi). Responses of many neurons during the Set-Go epoch were temporally scaled with respect to t_s (i.e., stretched in time for longer t_s), an effect that was most conspicuous as a change of slope among the

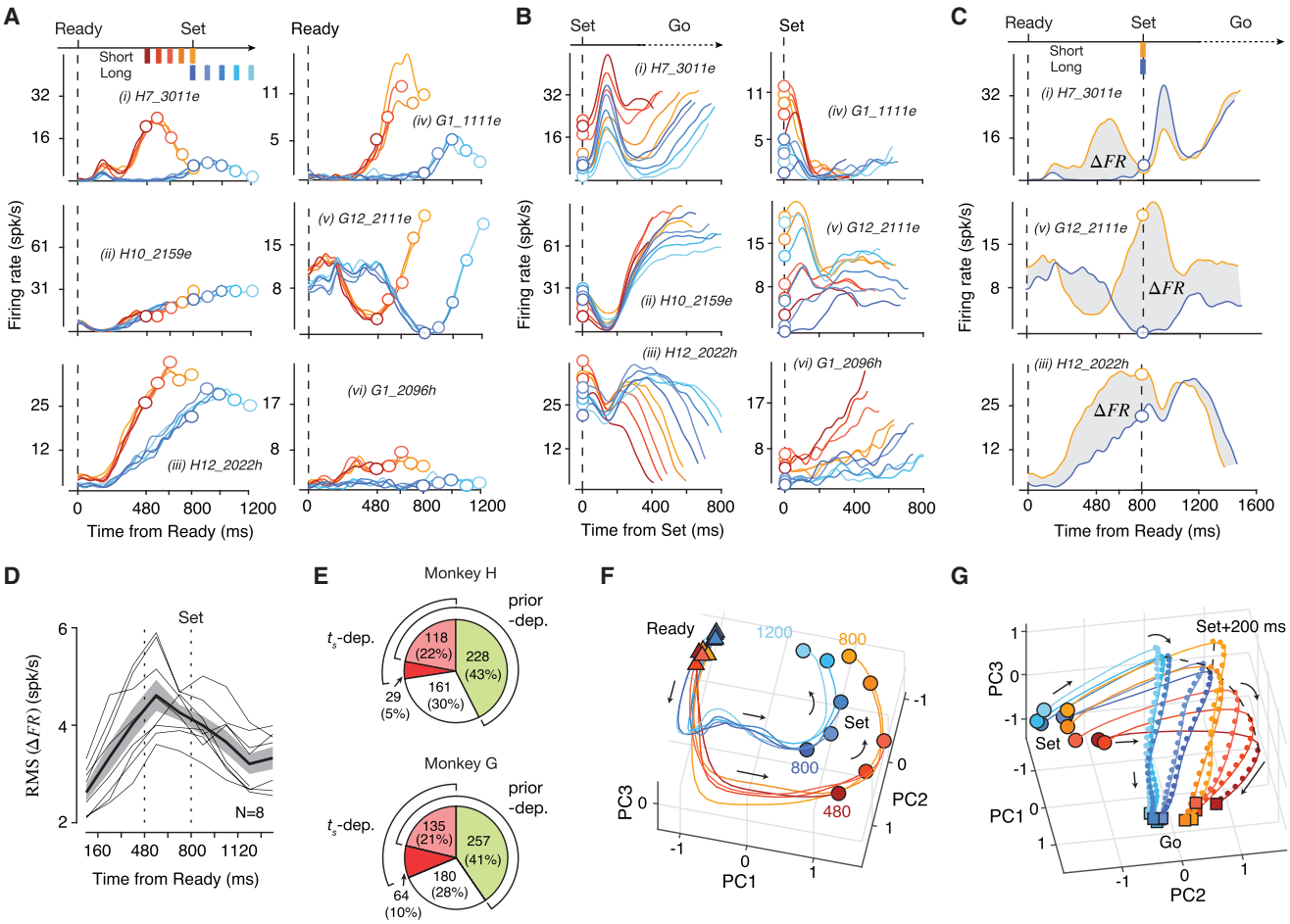

Figure 3. DMFC Response Profiles and Neural Trajectories

(A) Firing rate of 6 example neurons (i-vi) during the estimation epoch for Short (shades of red) and Long (shades of blue) prior conditions aligned to the time of Ready (vertical dashed line), and Set (open circles). Top left: the support of the prior. Labels (e.g., H7_3011e) indicate the animal (H versus G) and the effector (e for Eye and h for Hand).

(B) Same as (A) during the production epoch. Due to animals' behavioral variability, production epochs for the same t_s were of different durations. The plot shows the average activity of neurons from the time of Set (vertical dashed line) to the minimum t_p for each t_s.

(C) Firing rate of 3 of the neurons in (A) throughout the trial for the overlap t_s of 800 ms (Short: orange, Long: blue). The shaded area shows the difference in firing rates between the two prior conditions (ΔFR).

(D) Root-mean-squared (RMS) of ΔFR during the trial (bin size: 160 ms; thin gray line: data from 2 animals × 2 effectors × 2 directions; thick black line, mean across 8 datasets; shaded area, SEM).

(E) Pie chart of the percentage of neurons with activity dependent on the prior ("prior-dep.") and/or t_s ("t_s-dep."), determined by a generalized linear model (green, only prior-dependent, dark red, only t_s-dependent, light red: both prior- and t_s-dependent, white: the remaining neurons).

(F) Neural trajectories during the estimation epoch for a representative dataset (monkey H, Eye Left condition) in the subspace spanned by the first three principal components (PCs) with the same color scheme as (A) (triangles, Ready; circles, Set; arrows, temporal evolution of trajectories).

(G) Same as (F) for the production epoch (circles, Set; squares, Go). Trajectories were truncated at the minimum t_p for each t_s (dashed line, neural states 200 ms after Set; small dots, neural states at 20-ms increments). The distance between consecutive dots reflects speed.

See Figure S3 for other datasets.

subset of ramping neurons (Figure 3Bii,vi). This temporal scaling is consistent with recent recordings in this area in a range of simple motor timing tasks (Emmons et al., 2017; Merchant et al., 2011; Mita et al., 2009; Remington et al., 2018a; Wang et al., 2018).

The influence of prior was most evident at the overlap t_s of 800 ms (Figure 3C). Despite identical task demands and temporal contingencies, many neurons had highly distinct firing rate patterns depending on the prior condition, with a maximum difference in firing rate during the support of the prior between 480 and 800 ms (Figure 3D). Remarkably, this effect was present immediately after block transitions (Figure S2). We used a generalized linear model (GLM) to quantify the influence of t_s and prior condition on spike counts (Figure 3E; see STAR Methods). Results indicated that approximately 30% of neurons were modulated by elapsed time (27% monkey H, 31% monkey G), and more than 60% were sensitive to the prior condition (65% monkey H, 62% monkey G). These results suggest that neural

responses during the support of the prior were shaped by a combination of the animal's prior belief and the measured interval, which are the two key ingredients for computing the Bayesian estimate of t_s.

Geometry and Dynamics of Population Activity

The relationship between neurons with complex activity profiles and the computations they perform may be understood through population-level analyses that depict their collective dynamics as neural trajectories (Buonomano and Maass, 2009; Churchland et al., 2012; Fetz, 1992; Rabinovich et al., 2008; Remington et al., 2018b; Shenoy et al., 2013). Recent work has used this approach to elucidate neural computations in a wide range of motor and cognitive tasks (Carnevale et al., 2015; Hennequin et al., 2014; Mante et al., 2013; Michaels et al., 2016; Rajan et al., 2016; Remington et al., 2018a; Rigotti et al., 2010; Wang et al., 2018). Following this line of work, we sought to understand the computational principles of Bayesian integration in the RSG task by analyzing the population activity in DMFC.

We applied principal component analysis (PCA) to study the evolution of neural trajectories for various experimental conditions. Our initial analysis indicated that neural responses associated with different effectors, target directions, and task epochs resided in different regions of the state space (Figure S4). Therefore, we applied PCA separately to neural responses across experimental conditions and task epochs. For all datasets, the population activity in each epoch was relatively low dimensional: 3–4 principal components (PCs) in the estimation epoch and 5–10 PCs in the production epoch explained nearly 75% of total variance (Figure S3).

In the estimation epoch, neural trajectories associated with the two prior conditions were at different initial states at the time of Ready and became progressively more distinct throughout their evolution (Figures 3F and S3; Video S1). A notable feature of population activity in this epoch was the presence of curved neural trajectories during the support of each prior; i.e., approximately between 480 and 800 ms in the Short prior and between 800 and 1,200 ms in the Long prior. The presence of this prior-specific curvature was consistent with responses of single neurons, many of which were selectively modulated during the support of each prior (Figure 3Ai,iii,iv). This feature was ubiquitous for all experimental conditions (Figure S3), although the corresponding neural activity patterns resided in different parts of the state space (Figure S4).

The curved portion of the trajectories associated with the two prior conditions were parallel in the state space, suggesting that they relied on similar patterns of activity (Figure S4). Notably, the subspace for the 480 to 800 ms of the Short prior was shared to a greater extent with the subspace for the 800 to 1,200 ms than the 480 to 800 ms of the Long prior ("Short In Long"; Figure S4). These findings are consistent with the observation that activity profiles of single neurons during the support of the prior were similar across the two prior conditions (Figure 3A). These results highlight a potential link between the curvature and the neural representation of the prior.

In the production epoch, trajectories were at different initial states at the time of Set (Figure 3G; Video S2). The Set flash caused a rapid displacement of neural states, after which neural states evolved toward a terminal state (Go) at a progressively slower rate for longer t_s (Figure 3G). The prior-dependent initial conditions, the Set-triggered transient response, and the t_s-dependent rate of evolution of firing rates were all evident in the responses of many single neurons (Figure 3B). Both the role of speed in the control of movement initiation time (Wang et al., 2018) and the importance of initial state in adjusting the speed (Remington et al., 2018a) have been demonstrated previously. The question that remains is how the brain establishes a sigmoidal mapping during the support of the prior so that the speed of the ensuing trajectories is appropriately biased according to Bayesian integration.

Bayesian Estimation through Latent Dynamics

A property of a curved trajectory is that when projected onto a line connecting its two ends, equidistant points along the trajectory become warped. In other words, points near the ends of the projected line become biased toward the middle (Figure 4A), which qualitatively matches the sigmoidal mapping predicted from the Bayesian model (Figure 2). Based on this realization, we hypothesized that the curvature of neural trajectories during the support of the prior provides a computational substrate for Bayesian estimation. According to this hypothesis, which we refer to as the "curved manifold hypothesis," the animal's Bayesian behavior can be understood in terms of two computational stages (Figure 4B): (1) neural states evolving along the curved trajectory during the support of the prior provide an implicit, instantaneous representation of the Bayesian estimate of t_s (t_e), and (2) this Bayesian estimate adjusts the speed of the neural trajectory in the production epoch, which, in turn, enables animals to optimally bias their responses.

Encoding Bayesian Estimate along Curved Trajectory during Prior Support

We asked whether projections of neural states along the curved trajectory onto a one-dimensional "encoding axis" could establish a sigmoidal mapping similar to the Bayesian estimator (Figure 2A). Naturally, the answer depends on the choice of the encoding axis. Based on our understanding of the geometry of the problem (Figure 4A), we reasoned that a good candidate for the encoding axis is the vector pointing from the states associated with the shortest to the longest t_s for each prior condition (u; Figure 4B). Neural projections onto u exhibited biases that matched the Bayesian model fitted to the behavior (R^2 = 0.993 for the Short prior, 0.996 for the Long prior; Figure 4C), and this match was specific to our choice of u (i.e., projection onto other randomly chosen vectors in the state space failed to produce a sigmoidal function, Figure S5). Indeed, the neural projections were better explained by the Bayesian model than a linear model for both priors (signed-rank test for root-mean-squared error [RMSE], $p = 0.008$ for the Short prior, $p = 0.008$ for the Long prior; Figure 4D). As a negative control, we also analyzed neural data in the Long prior condition during a period temporally matched to support of the Short prior ("Short In Long" in Figure 4D) and found no evidence of sigmoidal representations (two-way repeated-measures ANOVA for RMSE with the prior conditions and the models as factors, $F_{1,7} = 161.43$, $p < 10^{-5}$ for their interaction; post hoc signed-rank test between the Bayesian and linear models for Short In Long, $p = 0.74$).

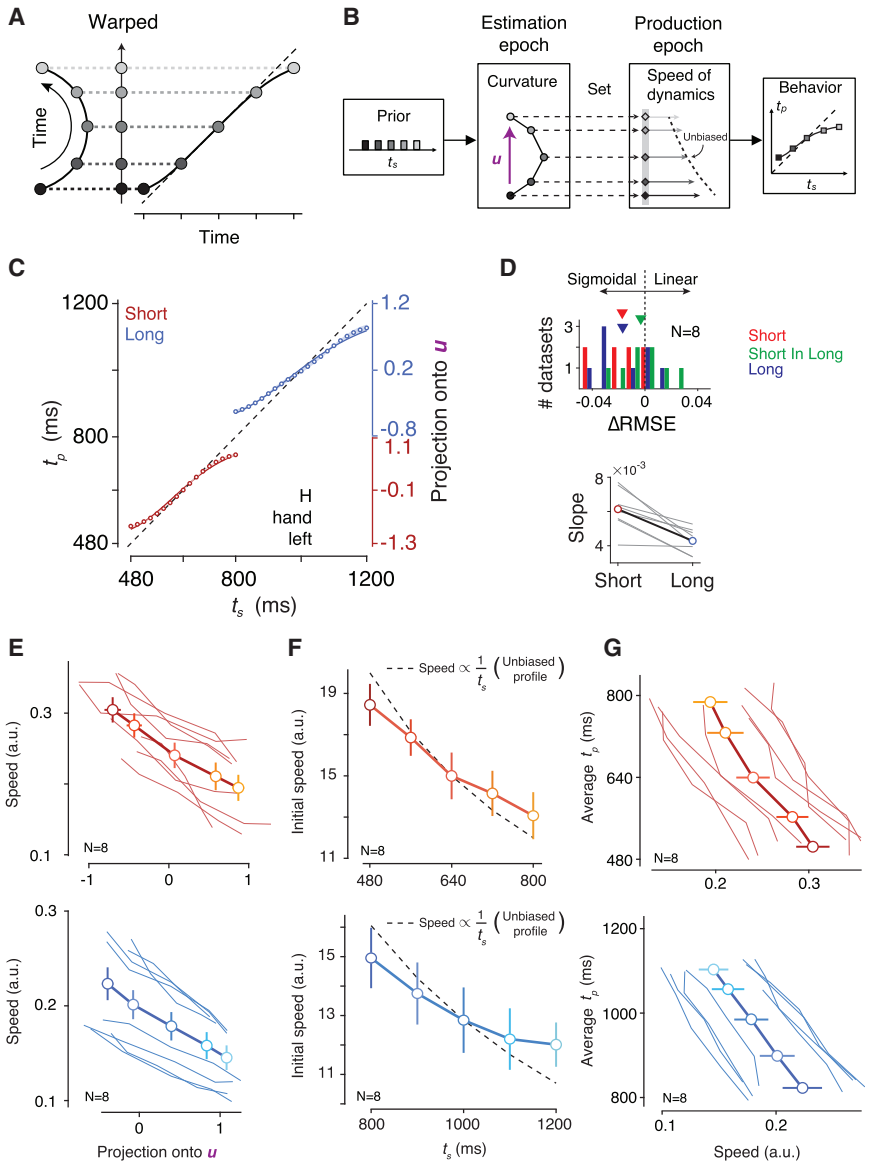

Figure 4. Neural Signatures of Bayesian Integration

(A) A geometric illustration of how linear projection of points along a 2D curve onto a 1D line could cause sigmoidal nonlinearity (gray dashed lines).

(B) The cascade of computations during the Ready-Set-Go task for different sample intervals (t_s). The prior distribution of t_s (leftmost panel) establishes curved trajectory during the estimation epoch (second leftmost panel). Projection of neural states along the curved trajectory onto an encoding axis (purple vector, u) creates a warped 1D representation of time that exhibits prior-dependent biases. In the ensuing production epoch (after the presentation of Set), the initial conditions (second rightmost panel; gray diamonds) reflect the warped representation of time and lead to biased speed profiles (dotted line, unbiased speed profile with $1/t_s$, see F). The biased speed profiles, in turn, allow the system to exhibit Bayes-optimal behavior (rightmost panel).

(C) Projection of neural states in the estimation epoch onto the encoding axis (u) as a function of t_s for a representative condition (monkey H, Hand Left condition) along the Bayesian model fit to behavior (line). Projections onto u (right ordinate axis) were linearly mapped onto the t_p range (left ordinate axis) with two free parameters for scaling and offset (circles, projections every 20 ms; red, Short; blue:, Long; shaded area, 95% bootstrap confidence intervals).

(D) Top: the difference between root-mean-squared error (ΔRMSE) of the Bayesian and linear model fits with the same number of free parameters (red, Short; blue, Long; green, Short in Long; see main text). Triangles at top show mean ΔRMSE averaged across individual datasets (2 animals × 2 effectors × 2 directions) for each prior condition. Bottom: regression slope relating neural projections to t_s for the Short and Long prior conditions (gray lines, individual datasets; black line with colored circles, mean).

(E) Speed of neural trajectories from Set to Go as a function of the projection of the neural state at Set onto u. The speed was estimated by averaging distances between successive bins of the states in the state space (thin lines, individual datasets across animals and conditions; thick line, average). Error bars are SEM.

(F) Speed profile across t_s within each prior. The dashed line represents the unbiased speed profile; we used the middle speed as reference, and scaled it according to each interval assuming constant traveling distance. To ensure that speed biases were already present early in the production epoch, speeds were computed as the average speed between Set and Set + 400 ms (i.e., initial speed). Results are presented in the same format as in (E).

(G) Average produced interval (t_p) as a function of speed at which neural states evolved during the production epoch. Results are presented in the same format as in (E).

A fundamental property of a Bayesian observer is that responses become more biased toward the mean of the prior when measurements are more uncertain (Figure 2G). As predicted, in the RSG task, we find larger behavioral biases for the Long prior condition (Figure 2H). Applying the same logic to the neural data, if projections onto the encoding vector represent t_e, they too should exhibit larger biases for the Long condition. A direct comparison of projected neural states between the two priors was consistent with this prediction: the Long prior exhibited more bias than the Short prior as measured by slope of a regression line relating projections to t_s (signed-rank test, $p = 0.008$; Figure 4D). Together, these results suggest that the curved trajectory in DMFC allow neural states to carry an implicit and instantaneous representation of t_e during the support of the prior.

Controlling Speed Based on Bayesian Estimate during the Set-Go Epoch

Previous work has demonstrated that flexible production of timed intervals is made possible through adjustments of the speed at which neural trajectories evolve toward an action-triggering state (Afshar et al., 2011; Churchland et al., 2008; Hanes and Schall, 1996; Wang et al., 2018). Accordingly, the

neural representations of t_e along the encoding axis should serve as initial conditions to dictate the speed during the ensuing production epoch (Figure 4B). We therefore examined the relationship between speed and neural projections on the encoding axis within each prior condition. For both conditions, larger projections along the encoding axis were associated with slower speeds across all conditions (Figure 4E; Pearson correlation, $\rho_{Short} = -0.74$, $p < 10^{-7}$, $\rho_{Long} = -0.51$, $p < 10^{-3}$). Crucially, we also tested whether speeds inherited biases from the warped organization of initial conditions at the time of Set. If Bayesian computation occurs during the support of the prior, speeds ought to incorporate the Bayesian biases immediately following Set. Accordingly, we computed the speed of neural trajectories early in the production epoch (i.e., initial speed) and examined the relationship between initial speed and t_s. An unbiased speed profile predicts that the speeds should be proportional to $1/t_s$. The speed profile for each prior condition, however, demonstrated systematic biases with a central tendency: trajectories associated with shorter t_s were slower than expected from an unbiased speed profile, and vice versa (Figure 4F; Wilcoxon sign-rank test on measured versus unbiased regression slopes relating speed to t_s, $p < 10^{-3}$ combining conditions and animals). This biased speed profile is fully consistent with the pattern seen in the behavior. Finally, we verified that the overall speed of dynamics throughout the production epoch was predictive of the resulting t_p across both priors and across all experimental conditions (Figure 4G; Pearson correlation, $\rho_{Short} = -0.58$, $p < 10^{-4}$, $\rho_{Long} = -0.52$, $p < 10^{-3}$). Together, these results support the curved manifold hypothesis according to which the curved trajectory supplies a Bayesian estimate of elapsed time, which controls the speed of dynamics during the production epoch allowing animals to produce Bayes-optimal behavior.

Alternative Mechanisms

We considered three alternative mechanisms that could, in principle, establish a Bayesian sigmoidal mapping.

Speed Hypothesis

Bayesian integration through modulation of speed in the estimation epoch. One way to create a sigmoidal warping is to have neural states near the two ends of the prior evolve more slowly than near the prior mean (Figure 5A). We tested this hypothesis by estimating the instantaneous speed of neural trajectories throughout the support of each prior. Results were not consistent with these predictions: for both prior conditions, speed remained unmodulated throughout the support of each prior (Figure 5B; signed-rank test for zero regression slopes during the support, $p = 0.64$ for Short, $p = 0.08$ for Long).

Transient Hypothesis

Bayesian integration by shaping the post-Set transient. Another way to create sigmoidal warping is to have the Set-triggered transient converge in the state space so as to elicit a bias in neural states toward the prior mean (Figure 5C). To test this alternative, we computed the distance between neural trajectories during the first 200 ms following Set. Results indicated that neural trajectories for different t_s in each prior evolved parallel to one another (signed-rank test for zero regression slopes relating the distance to time after Set, $p = 0.92$ for the shortest t_s, $p = 0.13$ for the longest t_s, across datasets and priors; Figure 5D; see also Figures 3G and S3). This suggests that the Set caused a t_s-independent transient response in DMFC that did not contribute significantly to the bias.

Threshold Hypothesis

Bayesian integration by establishing t_s-dependent movement thresholds. Finally, the biases could be induced by influencing the action-triggering state threshold (Figure 5E). If the threshold for fast trajectories (associated with shorter t_s) is pushed further away, the neural trajectories would have to travel a longer distance before reaching the action-triggering state, which would generate a positive bias. This model predicts, in particular, that states at the time of threshold-crossing should be different across t_s but more similar shortly before reaching the threshold due to speed differences (Figure 5E, left). The distance between neural trajectories should therefore decrease to a minimum before movement initiation and increase again to reflect the t_s-dependent threshold at the time of Go (Figure 5E, right). However, the distance profile of neural trajectories did not show this converging-diverging pattern; instead, the distance between trajectories appeared to drop steadily throughout the production epoch, even near the time of motor initiation (Figure 5F; one-tailed sign-rank test for time of minimum distance occurring strictly before movement initiation, $p = 1.5 \times 10^{-4}$, see Figure S5 for individual condition and animal).

The Curved Manifold Hypothesis Captures the Variance of Bayesian Estimates

Next, we asked whether the curved manifold hypothesis could additionally account for the variance of t_e. According to the Bayesian model, the variance of t_e as a function of t_s exhibits an inverted-U shape (Figure 6A): the sigmoidal mapping causes estimates near the extrema of the prior to be more biased and less variable than estimates near the mean of the prior, which are unbiased but more variable.

From a geometrical standpoint, neural states projected onto the encoding axis would be able to readily capture this inverted-U pattern if a sizeable portion of variance across trials is aligned to the curvature (Figure 6A). To test this possibility, we needed to derive accurate, trial-by-trial estimates of neural states. Such analysis is challenging but tractable if two conditions are concurrently met (Pandarinath et al., 2018; Williams et al., 2018; Yu et al., 2009): (1) data include sufficiently large number of simultaneously recorded neurons, and (2) neural trajectories are governed by a small number of latent factors. Under these assumptions, Gaussian process factor analysis (GPFA) can recover reliable estimates of single-trial neural trajectories (Afshar et al., 2011; Cowley et al., 2013; Yu et al., 2009).

We therefore focused our analysis on high-yield sessions ($n = 48$ for monkey H, $n = 107$ for monkey G) and used GPFA to extract high-fidelity, single-trial neural trajectories for the estimation epoch. We projected the neural states at the time of Set onto the encoding axis and computed the variance of the projections for each t_s separately (Figure 6B; see STAR Methods). The resulting variance profile of single-trial projections resembled an inverted U shape on average, with a tendency for lower variances at the extrema of each prior (one-tailed signed-rank test on coefficients for quadratic term in polynomial fitting, $p = 0.0273$, Figure 6C; see Figure S6 for

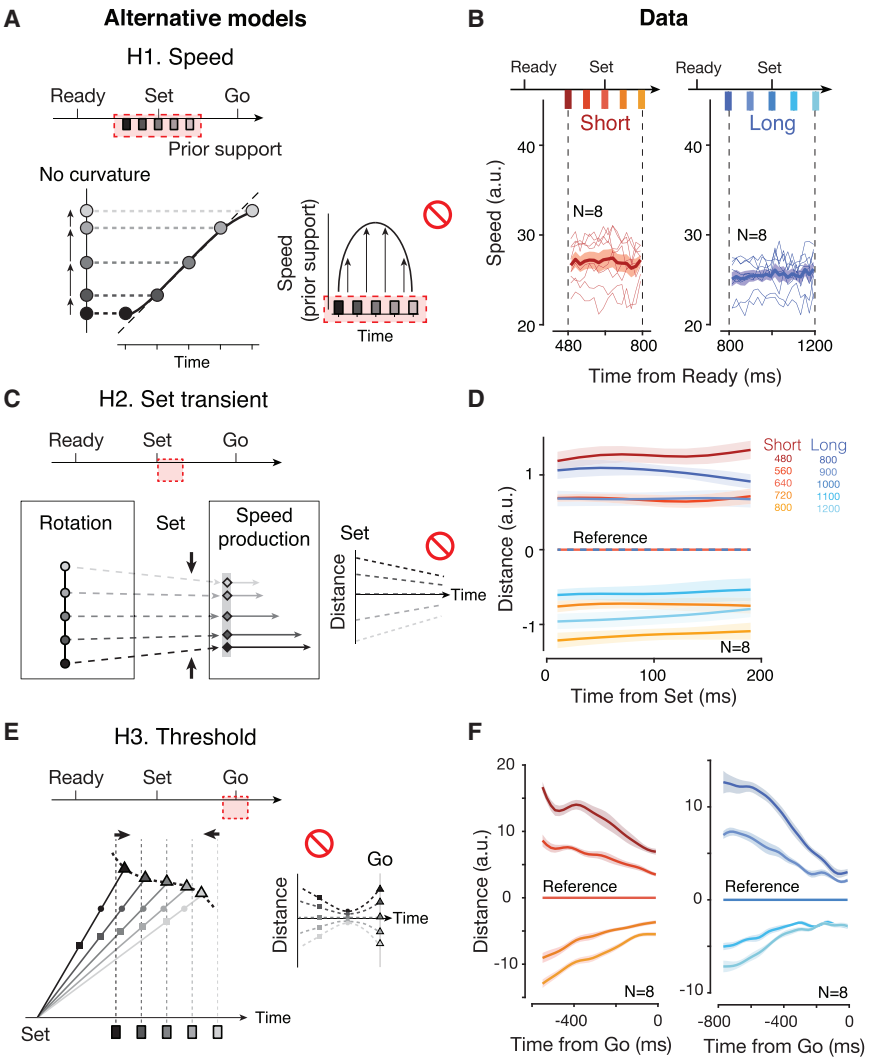

Figure 5. Alternative Mechanisms

(A) Speed model (H1). Top: Bayesian estimation during the support of the prior (shaded red) through modulation of speed. Bottom: if speed of neural trajectory is modulated according to an inverted U shape (accelerating then decelerating; right), projections off of the trajectory would exhibit regression to the mean (gray dashed lines).

(B) Instantaneous speed of neural trajectories during the estimation epoch for Short (red) and Long (blue) prior conditions computed in the full neural state space (thin lines, individual conditions for each animal; thick line, averages; shaded regions, SEM). Speeds were relatively constant during the support of the prior and did not follow the pattern predicted by H1.

(C) Transient model (H2). Top: Bayesian estimation through transient responses triggered by Set (shaded red). Bottom: the Set flash could push the system along slightly converging trajectories across t_s causing regress to the mean. This predicts a reduction of distance between consecutive trajectories shortly after Set (right).

(D) Distance between neural trajectories during the first 200 ms following Set. For each prior, we used the trajectory associated with the middle t_s as reference (horizontal lines at y = 0). For each time point along the reference trajectory, we computed the distance to the four other trajectories within each prior (shaded regions: SEM across datasets). Trajectories were analyzed using PCA between Set and Set + 200 ms across the two prior conditions (>75% variance explained). Distances were relatively fixed and did not converge as predicted by H2.

(E) Threshold model (H3). Top: Bayesian estimation through adjustment of threshold at the time of Go (shaded red). Bottom: if action-triggering states (curved dashed line) are biased such that faster trajectories (i.e., associated with shorter t_s) have to travel longer distances to reach the threshold, threshold-crossing times (triangles) would exhibit regression to the mean even with unbiased speeds (left). This predicts a distinctive nonmonotonic organization of neural trajectories: distances between trajectories associated with different t_s exhibit a large-small-large (squares-circles-triangles) pattern before the Go response (right).

(F) Distance between neural trajectories aligned to the motor response. Similar to (D), we used the middle trajectory as reference for the two prior conditions (left for Short, right for Long). Distances decreased monotonically and did not follow the distinctive pattern predicted by H3. Shaded area represents 95% confidence interval across conditions and animals. Distances were computed in the PC space obtained across t_s and accounted for ~60% of the total variance; results remained unchanged when more PCs were included.

See also Figure S5.

monkey G). This analysis indicates that the curved manifold hypothesis can additionally predict the second-order statistics of the Bayesian estimate. We also confirmed that the mean of the single-trial projections inferred from GPFA had a sigmoidal shape (signed-rank test between increments of mean *Xu* around extreme t_s versus those near middle t_s, p = 0.0078) and higher slope for the Short prior (one-tailed signed-rank test for regression slope between Short and Long, p = 0.0625; Figure 6D), consistent with results inferred from the trial-averaged firing rates (Figure 4C), and the behavior of the Bayesian estimator (Figures 2F and 2H). Finally, the single-trial neural state estimates derived from the GPFA analysis enabled us to validate the three-way relationship between neural states during the support of the prior (before Set), the speed of neural trajectories after Set, and the resulting t_p (Figure S6).

Recurrent Network Models of Cortical Bayesian Integration

RNN models have proven useful in elucidating how neural populations in higher cortical areas support various motor and cognitive computations (Mante et al., 2013; Rajan et al., 2016; Song et al., 2016; Sussillo et al., 2015; Yang et al., 2019). To gain further insight into how neural systems implement Bayesian inference, we trained RNNs to perform the two-prior RSG task (Figure 7A). On each trial, the network received a fixation cue as a tonic input whose value was adjusted by the prior condition.

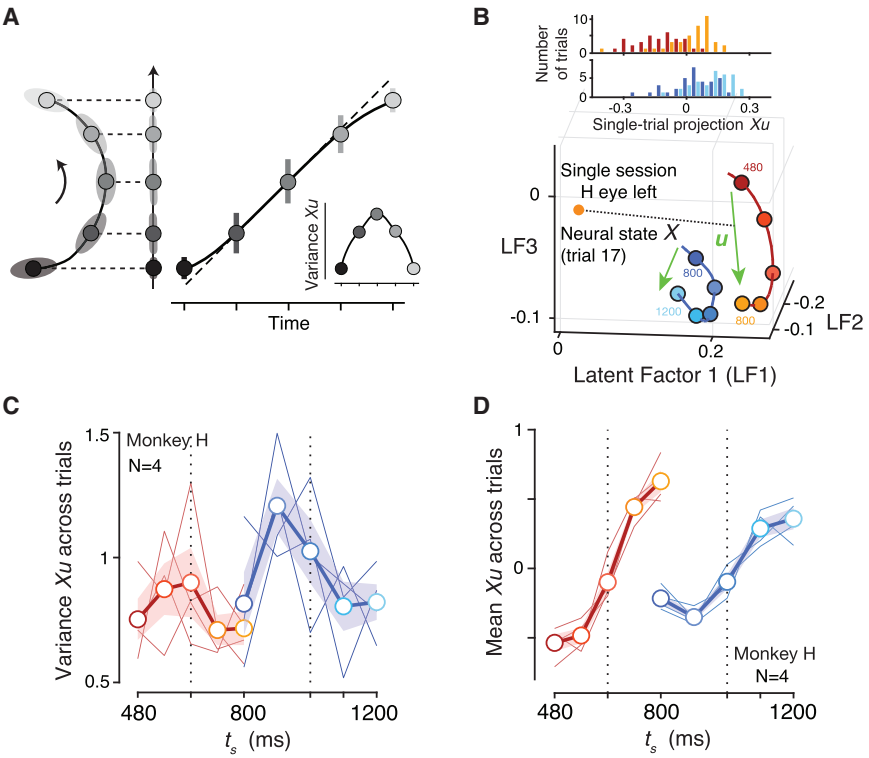

Figure 6. Trial-by-Trial Analyses

(A) A geometric interpretation of how a curved neural trajectory could establish the bias-variance trade-off expected from the sigmoidal Bayesian estimator in our task. Curvature causes neural states near the two ends to be mapped onto a relatively narrow range (smaller error bars). This squashes variability and predicts an inverted-U profile for variance of neural projections (Xu) as a function of t_s (inset).

(B) Single-trial estimate of neural states (X). Bottom: neural trajectories during the support of the Short (red) and Long (blue) prior conditions based on neural state estimates derived from a Gaussian process factor analysis (GPFA; see STAR Methods). Top: neural states for each t_s projected onto the encoding axis (u).

(C) Variance of projected neural states (Xu) across t_s. We Z-scored Xu of all trials before computing the variance for each t_s (thin lines: individual conditions; thick line: averages across conditions; shaded area: SEM across conditions).

(D) Projected neural states averaged across single-trials as a function of t_s for both priors.

See also Figure S6.

A second input administered the Ready and Set via two pulses that were separated by t_s. The network was trained to generate a linear ramping signal during Set-Go that would reach a fixed threshold ("Go") at the correct time to reproduce t_s. Using a suitable training strategy (see STAR Methods), we were able to build RNNs whose behavior was captured by a Bayesian observer model (Figure 7B).

Like DMFC neurons, RNN units displayed heterogeneous response profiles and were strongly modulated during the support of the prior (Figure S7). Similar to DMFC, the overall network activity was low dimensional during both the estimation and production epochs (Figure S7). Most importantly, network population trajectories exhibited the geometric features of neural trajectories in DMFC. For instance, the network trajectories also exhibited curvature during the support of the prior (Figures 7C and S7). Finally, during the production epoch, the initial condition and speed of trajectories were organized by t_s (Figure 7C).

Next, we developed an on-manifold perturbation protocol to probe the causal link between the curved manifold and Bayesian integration. We allowed the network to evolve during the Ready-Set epoch, suspended the dynamics shortly before Set, placed the network into a desired altered state, and released the network to observe the effect of this perturbation on the behavior (see STAR Methods for control experiments). The perturbation was designed to systematically displace neural states along the encoding axis—a strategy that we refer to as re-encoding. We reasoned that, if indeed the curved manifold and the encoding vector u are responsible for warping the neural representations of time, then perturbing the network states along the manifold should alter the behavior in a predictable manner.

Using this strategy, we perturbed the network activity in two ways: (1) compression along u toward the middle t_s (mean of the prior), and (2) linear translation along u. According to our hypothesis, the projection of activity along u provides an implicit representation for the Bayesian estimate of t_s. The compression should therefore lead to increased bias toward the mean t_s (Figure 7D). The translation, on the other hand, should result in a systematic shift in the values of t_p toward longer or shorter intervals (Figure 7E) depending on the direction of the translation. Results confirmed these predictions: t_p values exhibited progressively larger regression to the mean for larger compressive perturbations (Figure 7D) and underwent an overall upward or downward shift as a result of translation (Figure 7E). These *in silico* experiments provide additional evidence for a potential causal role of the curved manifold in Bayesian computation.

DISCUSSION

The central challenge in understanding Bayesian computations is the need for a framework that can bridge explanations across multiple scales. Most previous studies sought to understand Bayesian integration at the level of single neurons. This was also our starting point. We found that prior beliefs and sensory measurements concurrently modulated the firing rates of single neurons (Figure 3). Many previous studies have made similar observations. For example, some studies found that the stochastic nature of spiking activity in single neurons could provide the means to implicitly encode sensory likelihoods (Jazayeri and Movshon, 2006; Ma et al., 2006). Others found that task-related firing rates of single neurons before the presentation of sensory information may be modulated by prior expectations (Basso and Wurtz, 1997; Rao et al., 2012), and firing rates after

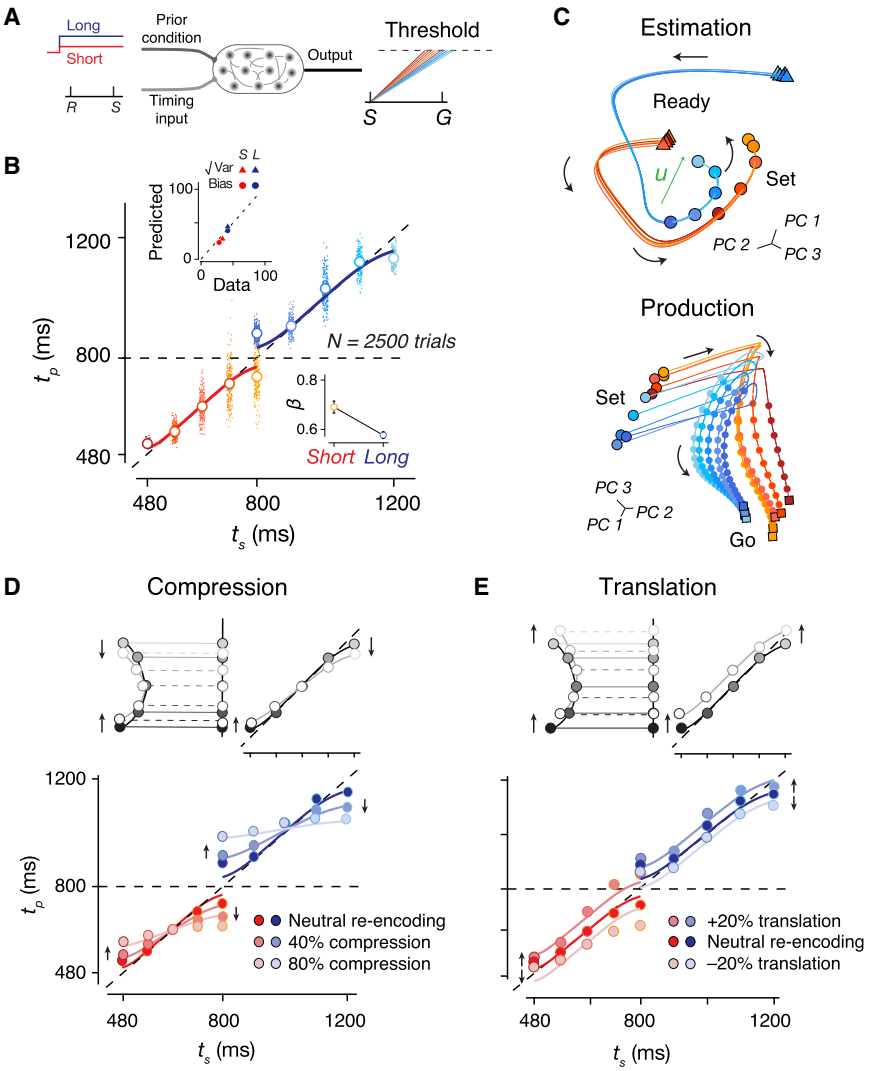

Figure 7. RNN Model of Bayesian Integration

(A) Schematic of RNN experimental design. RNN received two inputs. One provides a tonic input encoding the prior condition (Short: red; Long: blue), and the other supplies two pulses representing Ready (R) and Set (S). The network was trained to generate a linearly ramping output whose slope was inversely related to the sample interval between R and S (t_s). The Go response (G) was elicited when the output reached a threshold (dashed line). The production interval (t_p) was measured as the time between S and G.

(B) Network behavior shown using the same format as in Figure 1E. Inset top: bias (circles) and variance (triangles) of network responses compared to that of a Bayesian model for the Short (red) and Long (blue) prior conditions using the same procedure as Figures 2C and 2D. Inset bottom: regression coefficient analysis for the two priors (same color scheme) for different network runs.

(C) Network unit trajectories shown using the same format as Figures 3F and 3G.

(D) Top: schematic showing perturbed states (white circle) that are compressed toward the state associated with the mean t_s (arrows) relative to the original states (gray circles). Bottom: network behavior with no compression (dark hue, neutral re-encoding), with 40% compression (intermediate hue, and with 80% compression (light hue) for the Short (red) and Long (blue) prior conditions. Solid lines represent corresponding fits to the Bayesian model.

(E) Same as (D) for translational perturbation with either 20% positive translation along the moving trajectory or 20% negative translation against the moving trajectory. Solid lines represent the Bayesian model translated by an offset.

See also Figure S7.

the presentation of sensory information may reflect Bayesian estimate of behaviorally relevant variables (Beck et al., 2008; Funamizu et al., 2016; Hanks et al., 2011; Jazayeri and Shadlen, 2015). There have also been attempts to apply reliability-weighted linear updating schemes—commonly used in cue combination studies (Angelaki et al., 2009; Fetsch et al., 2009; Gu et al., 2008)—to explain how single-neurons might combine sensory evidence with prior expectations (Darlington et al., 2018; Orban de Xivry et al., 2013). Together, these results have provided valuable insights into single-neuron representations of prior beliefs and sensory measurements. However, probing the system at the level of single neurons has not led to a principled understanding of the computational logic that populations of neurons implement to perform Bayesian integration.

To address this challenge, we investigated population neural activity using a framework that is rooted in the language of dynamical systems. The behavior of a dynamical system is constrained by the coupling between interacting variables in the system (Remington et al., 2018b). Recent theoretical studies have found that the same framework can be used to explain how synaptic coupling between neurons constrains the population activity pattern across a network of recurrently interacting neurons. In particular, it has been shown that structured connectivity in RNN models establishes low-dimensional manifolds with powerful computational capacities (Mastrogiuseppe and Ostojic, 2018) for integration (Wang, 2008), categorization (Chaisangmongkon et al., 2017), gating (Mante et al., 2013), timing (Goudar and Buonomano, 2018; Laje and Buonomano, 2013; Remington et al., 2018a; Wang et al., 2018), learning (Athalye et al., 2017; Golub et al., 2018; Sadtler et al., 2014), movement control (Gallego et al., 2017; Hennequin et al., 2014; Kaufman et al., 2014; Michaels et al., 2016; Shenoy et al., 2013; Sussillo et al., 2015), and forming addressable memories (Hopfield, 1982). According to this framework, the computations that a neural system performs can be understood through an analysis of the geometry and dynamics of activity across the population (Gallego et al., 2017, 2018; Remington et al., 2018a; Sussillo, 2014).

Using this approach, we found a simple computational principle for how neural circuits perform Bayesian integration. We found that prior statistics that were presumably embedded in

the coupling between neurons, established low-dimensional curved manifolds across the population. This curvature, in turn, warped the underlying neural representations giving rise to biased responses consistent with Bayes-optimal behavior. This mechanism was evident across multiple behavioral conditions including different prior distributions and different effectors suggesting that it may entail a general computational strategy for Bayesian integration.

Notably, the curved manifold not only explained the prior-dependent bias but also accounted for the drop in variance of single-trial Bayesian estimates near the extrema of the prior, consistent with the predictions of a Bayesian estimator. The fact that the variance of projected states as a function of t_s exhibits an inverted-U shape suggests that a large fraction of variability occurs along the trajectory (Figure 6A). This implies, in turn, that one of the main contributors of noise in the system might be the speed of the trajectory (Hardy et al., 2018; Mello et al., 2015; Wang et al., 2018).

This computational strategy also emerged in an RNN model trained on the same task. While previous work has demonstrated that artificial network models can perform a variety of sensory, motor, and decision-making tasks (Chaisangmongkon et al., 2017; Mante et al., 2013; Remington et al., 2018a; Wang et al., 2018; Yang et al., 2019), training networks to encode and integrate prior beliefs has remained a challenge. Relying on our understanding of the importance of signal-dependent noise in timing (Hardy et al., 2018; Mello et al., 2015; Wang et al., 2018), we were able to create a suitable training strategy that allowed the networks to integrate prior beliefs. In particular, we found that, among multiple training regimes with different types of noises (see STAR Methods), introduction of external noise mimicking scalar measurement variability was key to inducing the prior-dependent bias in the network.

One of the most highly sought-after advancements in systems neuroscience is an ability to exert full control over neural activity, which would allow the experimenter to investigate the behavioral and neural consequences of setting the population activity to a specific state (Jazayeri and Afraz, 2017). This is currently impossible because we do not have a technique that can adjust the firing rates of many neurons concurrently, although notable efforts in this direction have been made (Bashivan et al., 2019; O'Connor et al., 2013; Ponce et al., 2019). The possibility of such concurrent modification would be extremely valuable in further testing the merits of our curved manifold hypothesis, as it would allow us to validate whether neural states along the curved trajectory truly encode the animal's internal estimates. Although it was not possible to perform this experiment *in vivo*, establishing an RNN model of Bayesian integration allowed us to causally probe potential underlying mechanisms by performing such targeted population-level perturbations *in silico*. The results of these experiments validated two key aspects of the curved manifold hypothesis: the orderly organization of the Bayesian estimates along the trajectory, and the role of the curvature in inducing regression toward the mean of the prior. Given the overall similarities of *in vivo* and *in silico* networks in terms of the response properties associated with Bayesian integration (Figures 7 and S7), this causal validation of the mechanism *in silico* provides tantalizing evidence that future experiments may find analogous results *in vivo*.

To put our findings in perspective, it is important to distinguish between the classic formulation of Bayes-optimal integration and the various algorithms the brain might use to optimize behavior in accordance with Bayesian theory. The classic formulation of Bayesian integration defines the likelihood function and prior probability distribution explicitly and uses them to compute a posterior distribution from which an optimal estimate can be inferred depending on a desired cost function. However, the derivation of optimal estimates from sensory measurements can be implemented by numerous isomorphic computational algorithms that do not necessarily depend on an explicit representation of the likelihood and/or the prior (Fiser et al., 2010; Ma and Jazayeri, 2014; Raphan and Simoncelli, 2006). Indeed, theoretical (Simoncelli, 2009) and behavioral (Acerbi et al., 2012; Jazayeri and Shadlen, 2010; Stocker and Simoncelli, 2006) studies have highlighted that Bayes-optimal behavior can be implemented by simple deterministic functions that map noisy measurement to optimal estimates. Our work supports this hypothesis; it shows that recurrent interactions between neurons establish manifolds whose geometry confers upon the population activity patterns an implicit representation of the optimal estimate without relying on explicit representations of the prior distribution and/or the likelihood function.

Although we focused on Bayesian integration in the domain of time, the key insights gleaned from our results may apply more broadly to perception, sensorimotor function, and cognition. For example, numerous studies have found an important role for natural scene statistics in vision and have shown that the organization of tuning in neurons of the primary visual cortex follows those statistics (Simoncelli and Olshausen, 2001). This observation is often explained in terms of efficient coding (Ganguli and Simoncelli, 2014; Simoncelli and Olshausen, 2001). In this framework, neurons form heterogeneous basis sets that are tuned to statistics of the environmental variables. In our timing task, we also found single neurons that developed flexible tuning for the support of each of the two priors (Figure 3). In other words, single neurons in our experiment also abided by the principles of efficient coding. However, our work goes beyond the representational notion of efficient coding and provides an understanding of how populations of neurons perform behaviorally relevant computations. In particular, our results suggest that statistical regularities in the environment create geometrically constrained manifolds of neural activity that can suitably perform Bayesian integration.

STAR★METHODS

Detailed methods are provided in the online version of this paper and include the following:

- KEY RESOURCES TABLE
- LEAD CONTACT AND MATERIALS AVAILABILITY
- EXPERIMENTAL MODEL AND SUBJECT DETAILS
- METHOD DETAILS
  - Two-Prior Time-Interval Reproduction Task
  - Electrophysiology

SUPPLEMENTAL INFORMATION

Supplemental Information can be found online at https://doi.org/10.1016/j.neuron.2019.06.012.

ACKNOWLEDGMENTS

H.S. and N.M. were supported by the Center for Sensorimotor Neural Engineering. D.N. was supported by the Rubicon Grant (2015/446-14-008) from the Netherlands Organisation for Scientific Research (NWO) and by the Marie Sklodowska Curie Reintegration Grant (PredOpt 796577). M.J. was supported by NIH (NINDS-NS078127), the Sloan Foundation, the Klingenstein Foundation, the Simons Foundation (542993SPI), the McKnight-Endowment Fund for Neuroscience, the National Science Foundation Center for Sensorimotor Neural Engineering (UWSC6200 BPO4405), and the McGovern Institute. The authors thank Seth Egger, Sujay Neupane, Eli Pollock, Michal De-Medonsa, and Sabbi Lall for their comments on the manuscript.

AUTHOR CONTRIBUTIONS

H.S. and M.J. conceived the *in vivo* experiments. H.S. collected the physiology data. D.N. and M.J. conceived the *in silico* experiments with recurrent neural networks. D.N. trained, simulated, and analyzed the networks. H.S. and N.M. analyzed the physiology data. M.J. supervised the project. All authors were involved in interpreting the results and writing the manuscript.

DECLARATION OF INTERESTS

The authors declare no competing interests.

Received: November 1, 2018
Revised: April 15, 2019
Accepted: June 13, 2019
Published: July 15, 2019

REFERENCES

Acerbi, L., Wolpert, D.M., and Vijayakumar, S. (2012). Internal representations of temporal statistics and feedback calibrate motor-sensory interval timing. PLoS Comput. Biol. *8*, e1002771.

Afshar, A., Santhanam, G., Yu, B.M., Ryu, S.I., Sahani, M., and Shenoy, K.V. (2011). Single-trial neural correlates of arm movement preparation. Neuron *71*, 555–564.

Akrami, A., Kopec, C.D., Diamond, M.E., and Brody, C.D. (2018). Posterior parietal cortex represents sensory history and mediates its effects on behaviour. Nature *554*, 368–372.

Angelaki, D.E., Gu, Y., and DeAngelis, G.C. (2009). Multisensory integration: psychophysics, neurophysiology, and computation. Curr. Opin. Neurobiol. *19*, 452–458.

Athalye, V.R., Ganguly, K., Costa, R.M., and Carmena, J.M. (2017). Emergence of Coordinated Neural Dynamics Underlies Neuroprosthetic Learning and Skillful Control. Neuron *93*, 955–970.

Bashivan, P., Kar, K., and DiCarlo, J.J. (2019). Neural population control via deep image synthesis. Science. Published online May 3, 2019. https://doi.org/10.1126/science.aav9436.

Basso, M.A., and Wurtz, R.H. (1997). Modulation of neuronal activity by target uncertainty. Nature *389*, 66–69.

Beck, J.M., Ma, W.J., Kiani, R., Hanks, T., Churchland, A.K., Roitman, J., Shadlen, M.N., Latham, P.E., and Pouget, A. (2008). Probabilistic population codes for Bayesian decision making. Neuron *60*, 1142–1152.

Berkes, P., Orbán, G., Lengyel, M., and Fiser, J. (2011). Spontaneous cortical activity reveals hallmarks of an optimal internal model of the environment. Science *331*, 83–87.

Buonomano, D.V., and Maass, W. (2009). State-dependent computations: spatiotemporal processing in cortical networks. Nat. Rev. Neurosci. *10*, 113–125.

Carnevale, F., de Lafuente, V., Romo, R., Barak, O., and Parga, N. (2015). Dynamic Control of Response Criterion in Premotor Cortex during Perceptual Detection under Temporal Uncertainty. Neuron *86*, 1067–1077.

Chaisangmongkon, W., Swaminathan, S.K., Freedman, D.J., and Wang, X.-J. (2017). Computing by Robust Transience: How the Fronto-Parietal Network Performs Sequential, Category-Based Decisions. Neuron *93*, 1504–1517.

Chen, L.L., and Wise, S.P. (1996). Evolution of directional preferences in the supplementary eye field during acquisition of conditional oculomotor associations. J. Neurosci. *16*, 3067–3081.

Churchland, A.K., Kiani, R., and Shadlen, M.N. (2008). Decision-making with multiple alternatives. Nat. Neurosci. *11*, 693–702.

Churchland, M.M., Cunningham, J.P., Kaufman, M.T., Foster, J.D., Nuyujukian, P., Ryu, S.I., and Shenoy, K.V. (2012). Neural population dynamics during reaching. Nature *487*, 51–56.

Coull, J.T., Vidal, F., Nazarian, B., and Macar, F. (2004). Functional anatomy of the attentional modulation of time estimation. Science *303*, 1506–1508.

Cowley, B.R., Kaufman, M.T., Butler, Z.S., Churchland, M.M., Ryu, S.I., Shenoy, K.V., and Yu, B.M. (2013). DataHigh: graphical user interface for visualizing and interacting with high-dimensional neural activity. J. Neural Eng. *10*, 066012.

Cui, X., Stetson, C., Montague, P.R., and Eagleman, D.M. (2009). Ready...go: Amplitude of the FMRI signal encodes expectation of cue arrival time. PLoS Biol. *7*, e1000167.

Darlington, T.R., Beck, J.M., and Lisberger, S.G. (2018). Neural implementation of Bayesian inference in a sensorimotor behavior. Nat. Neurosci. *21*, 1442–1451.

Emmons, E.B., De Corte, B.J., Kim, Y., Parker, K.L., Matell, M.S., and Narayanan, N.S. (2017). Rodent Medial Frontal Control of Temporal Processing in the Dorsomedial Striatum. J. Neurosci. *37*, 8718–8733.

Fetsch, C.R., Turner, A.H., DeAngelis, G.C., and Angelaki, D.E. (2009). Dynamic reweighting of visual and vestibular cues during self-motion perception. J. Neurosci. *29*, 15601–15612.

Fetz, E.E. (1992). Are movement parameters recognizably coded in the activity of single neurons? Behav. Brain Sci. *15*, 679–690.

Fiser, J., Berkes, P., Orbán, G., and Lengyel, M. (2010). Statistically optimal perception and learning: from behavior to neural representations. Trends Cogn. Sci. *14*, 119–130.

Fujii, N., Mushiake, H., and Tanji, J. (2002). Distribution of eye- and arm-movement-related neuronal activity in the SEF and in the SMA and Pre-SMA of monkeys. J. Neurophysiol. *87*, 2158–2166.

Funamizu, A., Kuhn, B., and Doya, K. (2016). Neural substrate of dynamic Bayesian inference in the cerebral cortex. Nat. Neurosci. *19*, 1682–1689.

Gallego, J.A., Perich, M.G., Miller, L.E., and Solla, S.A. (2017). Neural Manifolds for the Control of Movement. Neuron *94*, 978–984.

Gallego, J.A., Perich, M.G., Naufel, S.N., Ethier, C., Solla, S.A., and Miller, L.E. (2018). Cortical population activity within a preserved neural manifold underlies multiple motor behaviors. Nat. Commun. *9*, 4233.

Ganguli, D., and Simoncelli, E.P. (2014). Efficient sensory encoding and Bayesian inference with heterogeneous neural populations. Neural Comput. *26*, 2103–2134.

Girshick, A.R., Landy, M.S., and Simoncelli, E.P. (2011). Cardinal rules: visual orientation perception reflects knowledge of environmental statistics. Nat. Neurosci. *14*, 926–932.

Gold, J.I., Law, C.-T., Connolly, P., and Bennur, S. (2008). The relative influences of priors and sensory evidence on an oculomotor decision variable during perceptual learning. J. Neurophysiol. *100*, 2653–2668.

Golub, M.D., Sadtler, P.T., Oby, E.R., Quick, K.M., Ryu, S.I., Tyler-Kabara, E.C., Batista, A.P., Chase, S.M., and Yu, B.M. (2018). Learning by neural reassociation. Nat. Neurosci. *21*, 607–616.

Goudar, V., and Buonomano, D.V. (2018). Encoding sensory and motor patterns as time-invariant trajectories in recurrent neural networks. eLife *7*, e31134.

Griffiths, T.L., Kemp, C., and Tenenbaum, J.B. (2008). Bayesian Models of Cognition. In Cambridge Handbook of Computational Cognitive Modeling, R. Sun, ed. (Cambridge University Press), pp. 59–100.

Gu, Y., Angelaki, D.E., and Deangelis, G.C. (2008). Neural correlates of multisensory cue integration in macaque MSTd. Nat. Neurosci. *11*, 1201–1210.

Halsband, U., Ito, N., Tanji, J., and Freund, H.J. (1993). The role of premotor cortex and the supplementary motor area in the temporal control of movement in man. Brain *116*, 243–266.

Hanes, D.P., and Schall, J.D. (1996). Neural control of voluntary movement initiation. Science *274*, 427–430.

Hanks, T.D., Mazurek, M.E., Kiani, R., Hopp, E., and Shadlen, M.N. (2011). Elapsed decision time affects the weighting of prior probability in a perceptual decision task. J. Neurosci. *31*, 6339–6352.

Hardy, N.F., Goudar, V., Romero-Sosa, J.L., and Buonomano, D.V. (2018). A model of temporal scaling correctly predicts that motor timing improves with speed. Nat. Commun. *9*, 4732.

Hennequin, G., Vogels, T.P., and Gerstner, W. (2014). Optimal control of transient dynamics in balanced networks supports generation of complex movements. Neuron *82*, 1394–1406.

Histed, M.H., and Miller, E.K. (2006). Microstimulation of frontal cortex can reorder a remembered spatial sequence. PLoS Biol. *4*, e134.

Hopfield, J.J. (1982). Neural networks and physical systems with emergent collective computational abilities. Proc. Natl. Acad. Sci. USA *79*, 2554–2558.

Huerta, M.F., and Kaas, J.H. (1990). Supplementary eye field as defined by intracortical microstimulation: connections in macaques. J. Comp. Neurol. *293*, 299–330.

Janssen, P., and Shadlen, M.N. (2005). A representation of the hazard rate of elapsed time in macaque area LIP. Nat. Neurosci. *8*, 234–241.

Jazayeri, M., and Afraz, A. (2017). Navigating the Neural Space in Search of the Neural Code. Neuron *93*, 1003–1014.

Jazayeri, M., and Movshon, J.A. (2006). Optimal representation of sensory information by neural populations. Nat. Neurosci. *9*, 690–696.

Jazayeri, M., and Shadlen, M.N. (2010). Temporal context calibrates interval timing. Nat. Neurosci. *13*, 1020–1026.

Jazayeri, M., and Shadlen, M.N. (2015). A Neural Mechanism for Sensing and Reproducing a Time Interval. Curr. Biol. *25*, 2599–2609.

Kaufman, M.T., Churchland, M.M., Ryu, S.I., and Shenoy, K.V. (2014). Cortical activity in the null space: permitting preparation without movement. Nat. Neurosci. *17*, 440–448.

Kim, J., Ghim, J.-W., Lee, J.H., and Jung, M.W. (2013). Neural correlates of interval timing in rodent prefrontal cortex. J. Neurosci. *33*, 13834–13847.

Knill, D.C., and Richards, W. (1996). Perception as Bayesian Inference (Cambridge University Press).

Körding, K.P., and Wolpert, D.M. (2004). Bayesian integration in sensorimotor learning. Nature *427*, 244–247.

Laje, R., and Buonomano, D.V. (2013). Robust timing and motor patterns by taming chaos in recurrent neural networks. Nat. Neurosci. *16*, 925–933.

Lara, A.H., Cunningham, J.P., and Churchland, M.M. (2018). Different population dynamics in the supplementary motor area and motor cortex during reaching. Nat. Commun. *9*, 2754.

Lu, X., Matsuzawa, M., and Hikosaka, O. (2002). A neural correlate of oculomotor sequences in supplementary eye field. Neuron *34*, 317–325.

Ma, W.J., and Jazayeri, M. (2014). Neural coding of uncertainty and probability. Annu. Rev. Neurosci. *37*, 205–220.

Ma, W.J., Beck, J.M., Latham, P.E., and Pouget, A. (2006). Bayesian inference with probabilistic population codes. Nat. Neurosci. *9*, 1432–1438.

Malapani, C., and Fairhurst, S. (2002). Scalar Timing in Animals and Humans. Learn. Motiv. *33*, 156–176.

Mante, V., Sussillo, D., Shenoy, K.V., and Newsome, W.T. (2013). Context-dependent computation by recurrent dynamics in prefrontal cortex. Nature *503*, 78–84.

Martens, J., and Sutskever, I. (2012). Training Deep and Recurrent Networks with Hessian-Free Optimization. In Neural Networks: Tricks of the Trade. Lecture Notes in Computer Science, G. Montavon, G.B. Orr, and K.R. Müller, eds. (Springer Heidelberg), pp. 479–535.

Mastrogiuseppe, F., and Ostojic, S. (2018). Linking Connectivity, Dynamics, and Computations in Low-Rank Recurrent Neural Networks. Neuron *99*, 609–623.e29.

Matell, M.S., Meck, W.H., and Nicolelis, M.A.L. (2003). Interval timing and the encoding of signal duration by ensembles of cortical and striatal neurons. Behav. Neurosci. *117*, 760–773.

Matsuzaka, Y., Aizawa, H., and Tanji, J. (1992). A motor area rostral to the supplementary motor area (presupplementary motor area) in the monkey: neuronal activity during a learned motor task. J. Neurophysiol. *68*, 653–662.

Mello, G.B.M., Soares, S., and Paton, J.J. (2015). A scalable population code for time in the striatum. Curr. Biol. *25*, 1113–1122.

Merchant, H., Zarco, W., Pérez, O., Prado, L., and Bartolo, R. (2011). Measuring time with different neural chronometers during a synchronization-continuation task. Proc. Natl. Acad. Sci. USA *108*, 19784–19789.

Merchant, H., Pérez, O., Zarco, W., and Gámez, J. (2013). Interval tuning in the primate medial premotor cortex as a general timing mechanism. J. Neurosci. *33*, 9082–9096.

Michaels, J.A., Dann, B., and Scherberger, H. (2016). Neural Population Dynamics during Reaching Are Better Explained by a Dynamical System than Representational Tuning. PLoS Comput. Biol. *12*, e1005175.

Mita, A., Mushiake, H., Shima, K., Matsuzaka, Y., and Tanji, J. (2009). Interval time coding by neurons in the presupplementary and supplementary motor areas. Nat. Neurosci. *12*, 502–507.

Murakami, M., Vicente, M.I., Costa, G.M., and Mainen, Z.F. (2014). Neural antecedents of self-initiated actions in secondary motor cortex. Nat. Neurosci. *17*, 1574–1582.

Narain, D., Remington, E.D., Zeeuw, C.I.D., and Jazayeri, M. (2018). A cerebellar mechanism for learning prior distributions of time intervals. Nat. Commun. *9*, 469.

O'Connor, D.H., Hires, S.A., Guo, Z.V., Li, N., Yu, J., Sun, Q.-Q., Huber, D., and Svoboda, K. (2013). Neural coding during active somatosensation revealed using illusory touch. Nat. Neurosci. *16*, 958–965.

Ohmae, S., Lu, X., Takahashi, T., Uchida, Y., and Kitazawa, S. (2008). Neuronal activity related to anticipated and elapsed time in macaque supplementary eye field. Exp. Brain Res. *184*, 593–598.

Orban de Xivry, J.J., Coppe, S., Blohm, G., and Lefèvre, P. (2013). Kalman filtering naturally accounts for visually guided and predictive smooth pursuit dynamics. J. Neurosci. *33*, 17301–17313.

Pachitariu, M., Steinmetz, N., Kadir, S., Carandini, M., and Harris, K.D. (2016). Kilosort: realtime spike-sorting for extracellular electrophysiology with hundreds of channels. bioRxiv. https://doi.org/10.1101/061481.

Pandarinath, C., O'Shea, D.J., Collins, J., Jozefowicz, R., Stavisky, S.D., Kao, J.C., Trautmann, E.M., Kaufman, M.T., Ryu, S.I., Hochberg, L.R., et al. (2018). Inferring single-trial neural population dynamics using sequential auto-encoders. Nat. Methods *15*, 805–815.

Platt, M.L., and Glimcher, P.W. (1999). Neural correlates of decision variables in parietal cortex. Nature *400*, 233–238.

Ponce, C.R., Xiao, W., Schade, P.F., Hartmann, T.S., Kreiman, G., and Livingstone, M.S. (2019). Evolving Images for Visual Neurons Using a Deep

Generative Network Reveals Coding Principles and Neuronal Preferences. Cell *177*, 999–1009.

Rabinovich, M., Huerta, R., and Laurent, G. (2008). Neuroscience. Transient dynamics for neural processing. Science *321*, 48–50.

Rajan, K., and Abbott, L.F. (2006). Eigenvalue spectra of random matrices for neural networks. Phys. Rev. Lett. *97*, 188104.

Rajan, K., Harvey, C.D., and Tank, D.W. (2016). Recurrent Network Models of Sequence Generation and Memory. Neuron *90*, 128–142.

Rao, V., DeAngelis, G.C., and Snyder, L.H. (2012). Neural correlates of prior expectations of motion in the lateral intraparietal and middle temporal areas. J. Neurosci. *32*, 10063–10074.

Raphan, M., and Simoncelli, E.P. (2006). Learning to be Bayesian without supervision. Adv. Neural Inf. Process. Syst. *19*, 1145–1152.

Remington, E.D., Narain, D., Hosseini, E.A., and Jazayeri, M. (2018a). Flexible Sensorimotor Computations through Rapid Reconfiguration of Cortical Dynamics. Neuron *98*, 1005–1019.

Remington, E.D., Egger, S.W., Narain, D., Wang, J., and Jazayeri, M. (2018b). A Dynamical Systems Perspective on Flexible Motor Timing. Trends Cogn. Sci. *22*, 938–952.

Rigotti, M., Ben Dayan Rubin, D., Wang, X.-J., and Fusi, S. (2010). Internal representation of task rules by recurrent dynamics: the importance of the diversity of neural responses. Front. Comput. Neurosci. *4*, 24.

Sadtler, P.T., Quick, K.M., Golub, M.D., Chase, S.M., Ryu, S.I., Tyler-Kabara, E.C., Yu, B.M., and Batista, A.P. (2014). Neural constraints on learning. Nature *512*, 423–426.

Schall, J.D., Stuphorn, V., and Brown, J.W. (2002). Monitoring and control of action by the frontal lobes. Neuron *36*, 309–322.

Schlag, J., and Schlag-Rey, M. (1987). Evidence for a supplementary eye field. J. Neurophysiol. *57*, 179–200.

Seo, H., Cai, X., Donahue, C.H., and Lee, D. (2014). Neural correlates of strategic reasoning during competitive games. Science *346*, 340–343.

Shenoy, K.V., Sahani, M., and Churchland, M.M. (2013). Cortical control of arm movements: a dynamical systems perspective. Annu. Rev. Neurosci. *36*, 337–359.

Shook, B.L., Schlag-Rey, M., and Schlag, J. (1991). Primate supplementary eye field. II. Comparative aspects of connections with the thalamus, corpus striatum, and related forebrain nuclei. J. Comp. Neurol. *307*, 562–583.

Simoncelli, E.P. (2009). Optimal estimation in sensory systems. Cogn. Neurosci. *IV*, 525–535.

Simoncelli, E.P., and Olshausen, B.A. (2001). Natural image statistics and neural representation. Annu. Rev. Neurosci. *24*, 1193–1216.

Song, H.F., Yang, G.R., and Wang, X.-J. (2016). Training Excitatory-Inhibitory Recurrent Neural Networks for Cognitive Tasks: A Simple and Flexible Framework. PLoS Comput. Biol. *12*, e1004792.

Stocker, A.A., and Simoncelli, E.P. (2006). Noise characteristics and prior expectations in human visual speed perception. Nat. Neurosci. *9*, 578–585.

Sugrue, L.P., Corrado, G.S., and Newsome, W.T. (2004). Matching behavior and the representation of value in the parietal cortex. Science *304*, 1782–1787.

Sussillo, D. (2014). Neural circuits as computational dynamical systems. Curr. Opin. Neurobiol. *25*, 156–163.

Sussillo, D., Churchland, M.M., Kaufman, M.T., and Shenoy, K.V. (2015). A neural network that finds a naturalistic solution for the production of muscle activity. Nat. Neurosci. *18*, 1025–1033.

Wang, X.-J. (2008). Decision making in recurrent neuronal circuits. Neuron *60*, 215–234.

Wang, J., Narain, D., Hosseini, E.A., and Jazayeri, M. (2018). Flexible timing by temporal scaling of cortical responses. Nat. Neurosci. *21*, 102–110.

Werbos, P.J. (1990). Backpropagation through time: what it does and how to do it. Proc. IEEE *78*, 1550–1560.

Williams, A.H., Kim, T.H., Wang, F., Vyas, S., Ryu, S.I., Shenoy, K.V., Schnitzer, M., Kolda, T.G., and Ganguli, S. (2018). Unsupervised Discovery of Demixed, Low-Dimensional Neural Dynamics across Multiple Timescales through Tensor Component Analysis. Neuron *98*, 1099–1115.

Yang, G.R., Joglekar, M.R., Song, H.F., Newsome, W.T., and Wang, X.-J. (2019). Task representations in neural networks trained to perform many cognitive tasks. Nat. Neurosci. *22*, 297–306.

Yu, B.M., Cunningham, J.P., Santhanam, G., Ryu, S.I., Shenoy, K.V., and Sahani, M. (2009). Gaussian-process factor analysis for low-dimensional single-trial analysis of neural population activity. J. Neurophysiol. *102*, 614–635.

STAR★METHODS

KEY RESOURCES TABLE

REAGENT or RESOURCE	SOURCE	IDENTIFIER
Experimental Models: Organisms/Strains		
Rhesus macaque (*Macaca mulatta*)	Alpha genesis	N/A
Software and Algorithms		
MATLAB	MathWorks	RRID:SCR_001622; http://www.mathworks.com/products/matlab/
KiloSort	Pachitariu et al., 2016	RRID:SCR_016422; https://github.com/cortex-lab/Kilosort
Other		
CerePlex Direct	Blackrock Microsystems	https://blackrockmicro.com/neuroscience-research-products/neural-data-acquisition-systems/cereplex-direct-daq/
Plexon V-Probes	Plexon	https://plexon.com/products/plexon-v-probe/
Eyelink 1000 eye tracker	SR Research	RRID:SCR_009602; http://www.sr-research.com

LEAD CONTACT AND MATERIALS AVAILABILITY

Further information and requests for resources and reagents should be directed to and will be fulfilled by the Lead Contact, Mehrdad Jazayeri (mjaz@mit.edu). This study did not generate new unique reagents.

EXPERIMENTAL MODEL AND SUBJECT DETAILS

All experimental procedures conformed to the guidelines of the National Institutes of Health and were approved by the Committee of Animal Care at the Massachusetts Institute of Technology. Experiments involved two naive, awake, male behaving monkeys (species: M. mulatta; ID: H and G; weight: 6.6 and 6.8 kg; age: 4 years old). Animals were head-restrained and seated comfortably in a dark and quiet room, and viewed stimuli on a 23-inch monitor (refresh rate: 60 Hz). Eye movements were registered by an infrared camera and sampled at 1kHz (Eyelink 1000, SR Research Ltd, Ontario, Canada). Hand movements were registered by a custom single-axis potentiometer-controlled joystick whose voltage output was sampled at 1kHz (PCIe6251, National Instruments, TX). The MWorks software package (https://mworks-project.org) was used to present stimuli and to register hand and eye position. Neurophysiology recordings were made by 1-3 24-channel laminar probes (V-probe, Plexon Inc., TX) through a bio-compatible cranial implant whose position was determined based on stereotaxic coordinates and structural MRI scan of the two animals. Analysis of both behavioral and spiking data was performed using custom MATLAB code (Mathworks, MA).

METHOD DETAILS

Two-Prior Time-Interval Reproduction Task

Task Contingencies

Animals were trained on an interval-timing task that we refer to as the Ready-Set-Go (RSG) in which they had to measure a sample interval, t_s, and produce a matching interval t_p by initiating a saccade or by moving a joystick. Each experimental session consisted of 8 randomly interleaved conditions, 2 effectors (Hand and Eye), 2 movement targets (Left and Right), and 2 prior distributions of t_s (Long and Short).

Trial Structure

Each trial began with the presentation of a circle (diameter: 0.5 deg) and a square (side: 0.5 deg) immediately below it. Animals had to fixate the circle and hold their gaze within 3.5 deg of it. The square instructed animals to move the joystick to the central location. To aid the hand fixation, we briefly presented a cursor whose instantaneous position was proportional to the joystick's angle and removed it after successful hand fixation. Upon successful fixation and after a random delay (500 ms plus a random sample from an exponential distribution with mean of 250 ms), a white movement target was presented 10 deg to the left or right of the circle (diameter: 0.5 deg). After another random delay (250 ms plus a random sample from an exponential distribution with mean of 250 ms), the Ready and Set stimuli were flashed sequentially around the fixation cues (outer diameter: 2.2 deg; thickness: 0.1 deg; duration: 100 ms). The animal had to measure the sample interval, t_s, demarcated by Ready and Set, and produce a matching interval, t_p, after Set by making a saccade or by moving the joystick toward the movement target presented earlier (Go). Across trials, t_s was sampled from one of two discrete uniform prior distributions, each with 5 equidistant samples, a "Short" distribution between 480 and 800 ms (μ_{Short} = 640 ms, σ^2_{Short} = 8533 ms^2), and a "Long" distribution between 800 and 1200 ms (μ_{Long} = 1000 ms, σ^2_{Long} = 13333 ms^2).

The 4 conditions associated with the 2 effectors and 2 prior conditions were interleaved randomly across blocks of trials. For 15 out of 17 sessions, the block size was set by a minimum (3 and 5 trials for H and G, respectively) plus a random sample from a geometric distribution with a mean of 3 trials that was capped at a maximum (20 for H and 25 for G). The resulting mean ± SD block lengths were 4.0 ± 4.4 and 13.3 ± 3.1 trials for H and G, respectively. In 2 sessions in H, switches occurred on a trial-by-trial basis. Because animal G had more trouble switching between conditions, block switches involved a change of prior or effector but not both. The position of the movement target was randomized on a trial-by-trial basis. Throughout every trial, the fixation cue provided information about the underlying prior and the desired effector. One of the two fixation cues was colored and the other one was white. The animal had to respond with the effector associated with the colored cue (circle for Eye and square for Hand), and the cue indicated the prior condition (red for Short and blue for Long).

To receive reward, animals had to move the desired effector in the correct direction, and the magnitude of the relative error defined as $|t_p\text{-}t_s|/t_s$ had to be smaller than 0.15. When rewarded, reward decreased linearly with relative error, and the color of the response target changed to green. Otherwise, no reward was given and the target turned red. Trials were aborted when animals broke the eye or hand fixation prematurely before Set, used incorrect effector, moved opposite to the target direction, or did not respond within $3t_s$ after Set. To compensate for lower expected reward rate in the Long prior condition due to longer duration trials (i.e., longer t_s values), we set the inter-trial intervals of the Short and Long conditions to 1220 ms and 500 ms, respectively.

Electrophysiology

Recording

We recorded from 617 and 741 units in monkey H and G, respectively in the dorsomedial frontal cortex (DMFC), comprising supplementary eye field (SEF), presupplementary motor area (Pre-SMA), and dorsal portion of the supplementary motor area (SMA). No recordings were made in the medial bank. Regions of interest were selected according to stereotaxic coordinates with reference to previous studies recording from the SEF (Fujii et al., 2002; Huerta and Kaas, 1990; Schlag and Schlag-Rey, 1987; Shook et al., 1991) and Pre-SMA (Fujii et al., 2002; Matsuzaka et al., 1992), and the existence of task-relevant modulation of neural activity. Recorded signals were amplified, bandpass filtered, sampled at 30 kHz, and saved using the CerePlex data acquisition system (Blackrock Microsystems, UT). Spikes from single-units and multi-units were sorted offline using Kilosort software suites (Pachitariu et al., 2016). We collected 456 single-units (H:196, G:260) and 902 multi-units (H:421, G:481) in 69 penetrations across 29 sessions (H:17, G:12).

QUANTIFICATION AND STATISTICAL ANALYSIS

Analysis of Behavior

Model Free Analysis of Behavior

We analyzed behavior in sessions with simultaneous neurophysiological recordings (H: 17 sessions, 26189 trials, G: 12 sessions, 30777 trials). First, we used a probabilistic mixture model to exclude outliers from further analysis. The model assumed that each t_p was either a sample from a task-relevant Gaussian distribution or from a lapse distribution, which we modeled as uniform distribution extending from the time of Set to $3t_s$. We fit the mean and standard deviation of the Gaussian for each unique combination of session, prior condition, t_s, effector, and target directions. Using this model, we excluded any trial in which t_p was more likely sampled from the lapse distribution (3.84% trials in H and 5.7% trials in G).

We measured the relationship between t_p and t_s separately for each combination of prior, effector, and target direction in individual sessions using linear regression ($t_p = \beta t_s + \varepsilon$). Since t_p is more variable for larger t_s due to scalar variability, we used a weighted regression; i.e., error terms for each t_s were normalized by the standard deviation of the distribution of t_p for that t_s. We tested whether regression slopes were larger than 0 and less than 1 (Figures 1 and S1; Table S1).

Analysis of Behavior with a Bayesian Model

We fit a Bayesian observer model to behavioral data (Figure 2). The Bayesian observer measures t_s using a noisy measurement process that generates a variable measured interval, t_m. The measurement noise has a Gaussian distribution with a mean of zero and a standard deviation that scales with t_s with constant of proportionality w_m. The observer combines the likelihood function, $p(t_m|t_s)$, with the prior, $p(t_s)$, and uses the mean of the posterior, $p(t_s|t_m)$, to compute an estimate, t_e. For a uniform prior, and under scalar property of time measurements, the mapping between t_e and t_m is sigmoidal (Figure 2). The observer aims to produce t_e through another noisy process generating a variable t_p. We assumed that production noise scales with t_e with constant of proportionality w_p. For each prior, the model also included an offset term (b) to accommodate any overall bias in t_p. Using maximum likelihood estimation (MLE), we fit the 4 free parameters of the model (w_m, w_p, b_{Short}, and b_{Long}) to data for each animal, effector, and target directions after pooling across sessions (Table S3).

Analysis of Single- and Multi-Unit Activity

Most analyses were performed in a condition-specific fashion (2 priors, 5 t_s per prior, 2 effectors, and 2 directions). We excluded units for which we had less than 5 trials per condition, and units whose average firing rate was less than 1 spike/s. The remaining units included in subsequent analyses were 536 and 636 in H and G, respectively. To plot response profile of individual neurons (Figures 3A–3C), we smoothed averaged spike counts in 1-ms bins using a Gaussian kernel with a standard deviation of 25 ms.

Generalized Linear Model

We used a generalized linear model (GLM) to assess which neurons were sensitive to the prior and t_s. We modeled spike counts in an 80-ms window immediately before Set, r_{Set}, as a sample from a Poisson process whose rate was determined by a weighted sum of a binary indicator for prior (I_{prior}: 1 for Long, 0 for Short) and 5 binary indicators for t_s values (I_{ts}) associated with the Short prior for which we also knew the firing rate for the Long prior. The model was augmented by 2 additional binary indicators to account for independent influences of the effector ($I_{effector}$: 1 for Hand, 0 for Eye), and direction ($I_{direction}$:1 for Left, 0 for Right).

$$r_{set} = \sum_{j=1}^{5} \beta_{ts} I_{ts}(j) + \beta_{prior} I_{prior} + \beta_{effector} I_{effector} + \beta_{direction} I_{direction} \quad \text{Equation 1}$$

To get the most reliable estimate for the regression weights, we included spike counts based on all trials with attrition (i.e., firing rate at time t was computed from spikes in all trials in which Set occurred after t), and estimated β parameters of the model using MLE for all included neurons. To assess the significance of the effect of the prior condition, we used Bayesian information criteria (BIC) to compare the full model (Equation 1) to a reduced model that did not include a regressor for the prior (Equation 2):

$$r_{set} = \sum_{j=1}^{5} \beta_{ts} I_{ts}(j) + \beta_{effector} I_{effector} + \beta_{direction} I_{direction} \quad \text{Equation 2}$$

We also used a GLM to assess which neurons were sensitive to t_s. Since values of t_s were different between the priors, we used two distinct GLMs, one for data in the Short prior and one for the Long prior (Equation 3):

$$r_{set} = \sum_{j=1}^{5} \beta_{ts} I_{ts}(j) + \beta_{effector} I_{effector} + \beta_{direction} I_{direction} \quad \text{Equation 3}$$

Equation 3 has the same format as Equation 2 but was used to assess neural data in the two prior conditions separately. To identify the neurons that were sensitive to t_s, we used BIC to compare the t_s-dependent GLM (Equation 3) to a reduced GLM in which there was no sensitivity to t_s (Equation 4):

$$r_{set} = \beta_0 + \beta_{effector} I_{effector} + \beta_{direction} I_{direction} \quad \text{Equation 4}$$

Neurons were considered t_s-dependent if the BIC was lower in the full model either for the Short or for the Long prior condition (Figure 3).

Analysis of Population Neural Activity

Principal Component Analysis

To examine the trajectory of population activity in state space, we applied principal component analysis (PCA) to condition-specific, trial-averaged firing rates (bin size: 20 ms, Gaussian smoothing kernel width: 40 ms). Since neurons modulated during estimation and production epochs were largely non-overlapping (Figure S4), we performed PCA separately on the two epochs. We first constructed firing rate matrices of all neurons and time points [time points x neurons]. This yielded 16 matrices (2 priors x 2 effectors x 2 directions x 2 epochs). We then concatenated the matrices across the two prior conditions along the time dimension and applied PCA to each of the resulting 8 data matrices to find principal components (PCs) for each unique combination of effector and direction, separately in the two epochs.

In the estimation epoch, firing rates for each t_s were estimated with attrition (i.e., firing rate at time t was computed from spikes in all trials in which Set occurred after t). However, results were qualitatively unchanged if firing rates were estimated without attrition. In the production epoch, to accommodate different trial lengths (i.e., variable t_p), we estimated firing rates only up to the shortest t_p for each t_s. Neural trajectories in the two epochs were analyzed within the subspace spanned by the top PCs that accounted for at least 75% of total variance (Figure S3). We will use $\boldsymbol{X}(t)$ to refer to a neural state within the PC space at time t.

Analysis of Neural Projection

In the estimation epoch, we examined the curvature in neural trajectories during the support of each prior by projecting $\boldsymbol{X}(t)$ onto an 'encoding axis', u, defined by a unit vector connecting the state associated with the shortest t_s (t_{s_min}) to that with the longest t_s (t_{s_max}) for that prior. We denote the projected states by $\boldsymbol{X}u$. To reduce estimation error, we computed multiple difference vectors connecting $\boldsymbol{X}(t_{s\_min}+\Delta t)$ to $\boldsymbol{X}(t_{s\_max}-\Delta t)$ for every Δt = 20 ms, and used the average as our estimate of u. We used bootstrapping (resampling trials with replacement 1000 times) to compute 95% confidence interval for $\boldsymbol{X}u$. We quantified the similarity between $\boldsymbol{X}u$ and the Bayesian estimates (t_e) inferred from model fits to behavior using linear regression ($\boldsymbol{X}u = \alpha + \beta t_e$). Since we included spike counts across trials with attrition, there were nearly 5 times more data for the shortest t_s compared to the longest t_s within each prior. Accordingly, for each t_s, error terms were weighted by the number of data points included for that t_s (5 for the shortest t_s, 4 for the second shortest, and so forth). We then used the coefficient of determination (R^2) to assess the degree to which t_e was explained by the neurally inferred $\boldsymbol{X}u$. To further validate the warping hypothesis that $\boldsymbol{X}u$ encodes t_e, we tested whether any linear model of t_s ($\boldsymbol{X}u = \alpha + \beta t_s$) can fit $\boldsymbol{X}u$ better. The number of free parameters (α, β) were matched between the Bayesian and linear models as t_e was computed only from behavioral data. The model fit was compared in terms of Root Mean Squared Error (RMSE) between the actual and predicted $\boldsymbol{X}u$ for individual datasets (2 animals x 2 effectors x 2 directions). As a negative control of our analysis, we applied the same projection analysis to data of the Long prior from 480 ms to 800 ms after Ready, which corresponded to the support of the Short prior ('Short In Long'). We also compared the slope β for t_s between the two prior conditions

(Figure 4D) as we performed in the behavioral analysis (Figures 2G and 2H). Finally, we tested the specificity of our results with respect to the chosen u by performing the same analysis for 1000 randomly chosen encoding axes (u'), and comparing the corresponding R^2 values (Figure S5).

We examined two later links of the cascade model (Figure 4B) during the production epoch. A key component in the production epoch was the speed of the neural trajectory traveling the state space. For each dataset, we computed the speed as the average Euclidean distance (in the PC space accounting for at least 75% of the total variance) between neural states associated with successive bins (20 ms), divided by the duration separating Set and the time of Go. First, we related the trajectory speed to the projected state along the encoding axis (u) across the prior and t_s to test if the state served as an initial condition to set up the speed of the ensuing trajectory (Figure 4E). We then assessed how the speed during the production epoch was associated with the behavioral output, t_p (Figure 4G). We computed a correlation coefficient between the t_p averaged across trials of each dataset and the trajectory speed and tested its statistical significance ($p < 0.05$).

Test of Alternative Mechanisms

To test alternative neural models for generating bias (Figure 5), we focused on two main features of neural trajectories: speed and distance across trajectories of the different priors and t_s. We applied PCA as before but only to the period of interest for each alternative model (from Set to Set+200 ms for the 'Set transient model', from Go-800 ms to Go for the 'Threshold model'). For the 'Speed model', we estimated instantaneous speed of the trajectory in the full neural space to avoid any potential distortion by smoothing and PCA (Figure 5B). For distance metric, trajectory of the middle t_s (i.e., prior mean) was used as a reference from which the distance was computed (Figures 5D and 5F).

Analysis of Neural State Variance

To estimate variance of neural states across individual trials during the support of the prior (Figure 6A), we used the following procedure. 1) We estimated the single-trial neural trajectories by applying Gaussian Process Factor Analysis (GPFA) (Cowley et al., 2013; Yu et al., 2009) to data from simultaneously recorded neurons in a single session (n = 48 in H, n = 107 in G) with cross validation. GPFA allowed us to avoid arbitrarily selecting size of the smoothing kernel and to estimate shared variability across population of neurons. 2) We projected the single-trial states onto the encoding vector u (Figure 6B). 3) We calculated variance and mean of the neural projections for each t_s in each prior condition. We also used GPFA to obtain single-trial estimate of the trajectory speed during the production epoch. We examined correlation between the trial-by-trial speed and the neural projection (Figure S6) and correlation between the speed and t_p across trials (Figure S6). To ensure that our analysis correctly captured the trial-by-trial relationship between speed and t_p and not their co-dependence on t_s (Figures 4E and 4G), we measured correlations after z-scoring single-trial data for each t_s and used the total-least-squares algorithm to ensure that the estimation errors of both speed and t_p were taken into account.

Recurrent Neural Network

We constructed a randomly connected firing-rate recurrent neural network (RNN) model with N = 200 nonlinear units. The network dynamics were governed by the following equations:

$$\tau \dot{\mathrm{x}}(t) = -\mathrm{x}(t) + \sum \mathrm{J}\mathrm{r}(t) + \sum \mathrm{B}\omega(t) + \mathrm{c}_x + \rho_x(t) \quad \text{Equation 5}$$

$$\mathrm{r}(t) = \tanh(\mathrm{x}(t)) \quad \text{Equation 6}$$

$\mathrm{x}(t)$ is a vector containing the activity of all units and $\mathrm{r}(t)$ represents the firing rates of those units, obtained by a nonlinear transformation of x. Time t was sampled every millisecond for a total duration of $T = 3500$ ms. The time constant of decay (τ) for each unit was set to 10 ms. The unit activations also contain an offset c_x and white noise $\rho_x(t)$ sampled at each time step from zero-mean normal distributions with standard deviation lying in the range between 0.01 and 0.015. The matrix J represents recurrent connections in the network. The network received multi-dimensional input ω through synaptic weights $\mathrm{B} = [\mathrm{b}_c, \mathrm{b}_s]$. The input comprised of a prior-dependent context cue $\omega_c(t)$ and an input $\omega_s(t)$ that provided Ready and Set pulses. In $\omega_s(t)$ Ready and Set were encoded as 20 ms pulses with a magnitude of 0.4 that were separated by time t_m, where $t_m \sim N(t_s, t_s w_m)$. w_m represents the weber fraction by which the noise process scales. The amplitude of the prior-dependent context input $\omega_c(t)$ was set to 0.3 for the Short prior and 0.4 for the Long prior contexts. Networks produced a one-dimensional output $\mathrm{z}(t)$ through summation of units with weights w_o and a bias term c_z.

$$\mathrm{z}(t) = \mathrm{w}_o^T \mathrm{r}(t) + \mathrm{c}_z \quad \text{Equation 7}$$

Network Training

Prior to training, model parameters (θ), which comprised J, B,w_o, c_x, and c_z were initialized. Initial values of matrix J were drawn from a normal distribution with zero mean and variance $1/N$, following previous work (Rajan and Abbott, 2006). Prior to training, synaptic weights B and the initial state vector $\mathrm{x}(0)$ and unit biases c_x were drawn from a uniform distribution with range [-1,1]. The output

weights, w_o and bias c_z were initialized to zero. During training, model parameters were optimized by truncated Newton methods (Martens and Sutskever, 2012) using backpropagation-through-time (Werbos, 1990) by minimizing a squared loss function between the network output $z_i(t)$ and a target function $f_i(t)$, as defined by:

$$H(\theta) = \frac{1}{|T_{tr}I|}\sum_{I}\sum_{T_{tr}}(z_i(t) - f_i(t))^2 \quad \text{Equation 8}$$

Here i indexes different trials in a training set (I = different prior contexts x intervals (t_s) x repetitions (r_e)). T_{tr} represents the epoch within a trial that was used to compute $H(\theta)$ and here corresponds to the production epoch. Accordingly, the target function $f_i(t)$ was only defined in the production epoch. The value of $f_i(t)$ was zero during the Set pulse. After Set, the target function was governed by two parameters that could be adjusted to make $f_i(t)$ nonlinear, scaling, non-scaling, or approximately-linear:

$$f_i(t) = A\left(e^{t/\alpha t_s} - 1\right) \quad \text{Equation 9}$$

For the networks reported, $f_i(t)$ was an approximately-linear ramp function parametrized by $A = 3$ and $\alpha = 2.8$. Solutions were robust with respect to the parametric variations of the target function (e.g., nonlinear and non-scaling target functions). In trained networks, t_p was defined as the time between the Set pulse and when the output ramped to a fixed threshold $(z_i = 1)$.

During training, we employed three strategies to obtain robust solutions. In general, we injected three sources of variability: (1) Noise added to individual units in the RNN, (2) noise added to input, and (3) noise imposed by jittering the time of events (scalar variability). The third regime generated the most Bayes-consistent results. In this scheme, the RNNs were trained such that interval-dependent scalar noise was introduced into their observations (various trials $t_m \sim N(t_s, t_s w_m)$); however, the target was always held to be the mean of those likelihood functions (t_s). In other words, interval between the Ready and Set pulses varied across trials with the scalar noise (t_m) while the network was trained to generate a ramping output during the production epoch that would reach threshold at Set+t_s. Within this family of networks, we systematically varied two parameters (repeated across multiple networks), w_m (weber fraction of the scalar noise) and the variance of white noise added to individual units to regularize the training procedure. However, it was challenging to train networks under such scalar noise. Complete failure of training was common and only 40% of networks were able to generate biased estimates that were consistent with Bayesian predictions. Importantly, all the networks that succeeded in performing Bayesian integration established the curved manifold.

Network Causal Experiment

To evaluate the importance of the encoding axis on the behavior of the RNN at the time of Go, we performed a targeted perturbation experiment involving changes of the network state along the encoding axis (u) shortly before Set, which we refer to as 're-encoding'. We systematically altered network states along the u 20 ms before the onset of Set and examined the consequences of this perturbation on behavior. To verify our approach, we first performed a control experiment in which the perturbation was expected to have no appreciable effect on behavior. Specifically, we re-encoded the network state for each trial of each t_s to the expected state for that t_s under no perturbation (n = 3000 trials per re-encoding). In this control experiment, perturbation had no effect on behavior (as expected) when we used a protocol in which (i) we allowed the network to stabilize for 10 ms after re-encoding (on the same order as the time constant of individual units in the RNN), and (ii) administered the Set pulse 10 ms after stabilization (Figure 7D). Having established a working protocol for the re-encoding experiment, we performed two causal experiments involving compression and translation of network states on u.

For the compression experiments, we evaluated the network's behavior after applying various levels of compression (40% and 80%) to network states toward the mean state (i.e., the state associated with the mean of the prior). For the translation experiments, the same procedure was used except that the re-encoding involved a 20% shift in network states in the positive or negative directions (i.e., resulting in increasing or decreasing t_s) (Figure 7E). One constraint in the translation experiment was that the network could not tolerate large negative shifts (i.e., intervals shorter than 400 ms for the short prior and 800 ms for the long prior). Such translations placed the network state in regions of the state space in which the latent dynamics were no longer governed by the curved manifold.

DATA AND CODE AVAILABILITY

The published article includes all datasets generated or analyzed during this study. The code supporting the current study is available from the corresponding author on request.